The Impact of Midlevel Shear Orientation on the Longevity of and Downdraft Location and Tornado-Like Vortex Formation within Simulated Supercells

KEVIN GRAY[a] AND JEFFREY FRAME[a]

[a] *Department of Atmospheric Sciences, University of Illinois at Urbana–Champaign, Urbana, Illinois*

(Manuscript received 14 April 2021, in final form 27 August 2021)

ABSTRACT: Despite an increased understanding of environments favorable for tornadic supercells, it is still sometimes unknown why one favorable environment produces many long-tracked tornadic supercells and another seemingly equally favorable environment produces only short-lived supercells. One relatively unexplored environmental parameter that may differ between such environments is the degree of backing or veering of the midlevel shear vector, especially considering that such variations may not be captured by traditional supercell or tornado forecast parameters. We investigate the impact of the 3–6-km shear vector orientation on simulated supercell evolution by systematically varying it across a suite of idealized simulations. We found that the orientation of the 3–6-km shear vector dictates where precipitation loading is maximized in the storms, and thus alters the storm-relative location of downdrafts and outflow surges. When the shear vector is backed, outflow surges generally occur northwest of an updraft, produce greater convergence beneath the updraft, and do not disrupt inflow, meaning that the storm is more likely to persist and produce more tornado-like vortices (TLVs). When the shear vector is veered, outflow surges generally occur north of an updraft, produce less convergence beneath the updraft, and sometimes undercut it with outflow, causing it to tilt at low levels, sometimes leading to storm dissipation. These storms are shorter lived and thus also produce fewer TLVs. Our simulations indicate that the relative orientation of the 3–6-km shear vector may impact supercell longevity and hence the time period over which tornadoes may form.

SIGNIFICANCE STATEMENT: We explore how the orientation of the 3–6-km vertical wind shear vector impacts the longevity of and thus the potential for near-surface vortex formation within simulated supercell thunderstorms. Our investigation is significant because these impacts have been relatively unexplored and because the midlevel winds dictate where outflow surges develop within supercells. We found that the storm-relative location of outflow surges can affect the magnitude of the convergence beneath an updraft, the buoyancy of the air flowing into an updraft, and the potential tilting and undercutting of an updraft by outflow, all of which can influence supercell longevity and thus the potential for near-surface vortex formation.

KEYWORDS: Downbursts; Severe storms; Storm environments; Supercells; Tornadoes

1. Introduction

Tornadic supercells pose a threat to life and property, and thus the environments that produce these storms have drawn much attention from researchers. In the past few decades, our knowledge of ingredients favorable for the development of these storms has improved greatly (e.g., Brooks et al. 2019; Coniglio and Parker 2020) and forecasters now can generally identify environments supportive of tornadic supercells, sometimes several days in advance. Yet even with this increased understanding, it is still not always well understood why in one favorable environment many long-lived tornadic supercells may develop, while in a seemingly equally favorable environment only short-lived or nontornadic supercells develop (e.g., Erwin et al. 2016; Klees et al. 2016; Coffer et al. 2017; Flournoy et al. 2020; Markowski 2020). Surely, there are mesoscale factors unique to a given environment or geographical region that also influence storm longevity and tornado production, but perhaps there is still something unknown that differentiates some environments that produce long-lived tornadic supercells from those that do not.

A typical environment supportive of tornadic supercells is characterized by nonzero convective available potential energy (CAPE), minimal convective inhibition (CIN), strong deep-layer vertical wind shear oriented such that the shear vector crosses the initiating boundary at a large (~45°–60°) angle (Bluestein and Weisman 2000; Dial et al. 2010), strong low-level vertical wind shear leading to a long, curved low-level hodograph and hence large values of storm-relative helicity (SRH; usually calculated over the 0–1- or 0–3-km layers, or even shallower layers, such as 0–500 m, as suggested by Coffer et al. 2020), and low lifting condensation levels (LCLs; Thompson et al. 2003, 2004). We chose to investigate midlevel shear vector orientation since its potential impacts are relatively unexplored compared to those of many other environmental parameters.

Warren et al. (2017) used an idealized model to investigate how upper-level (above 6 km) wind shear impacts supercell morphology and found that when the upper-level shear vector backs with height, precipitation is enhanced in the rear flank of the storm and when the upper-level shear vector veers with height, precipitation is enhanced toward the forward flank. They also found that stronger upper-level shear led to faster storm motions and thus increased storm-relative inflow. Parker (2017) found that backing winds aloft do not disrupt or weaken

Corresponding author: Kevin Gray, kevintg2@illinois.edu

DOI: 10.1175/MWR-D-21-0085.1

the upward-directed perturbation pressure gradient force below the level of free convection, and that upper-level winds oriented more parallel to a synoptic or mesoscale initiating boundary can lead to more rapid upscale growth. Otherwise, the degree of backing or veering of the midlevel vertical wind shear vector has generally not been examined, especially how it may influence the location of hydrometeor fallout and downdrafts within a storm.

Recent observational work suggests that internal outflow surges may be instrumental in the development of in-storm boundaries and may aid in tornadogenesis. Finley and Lee (2004) documented up to three rear-flank downdraft surges prior to tornadogenesis in the 9 June 2003 Bassett, Nebraska, supercell. Lee et al. (2012) documented four rear-flank downdraft internal surges within 1 km of the 22 May 2010 Bowdle, South Dakota, tornado and suggest that the convergence produced as a surge wraps into the pre-tornadic circulation may aid in tornadogenesis. Marquis et al. (2012), through dual-Doppler wind syntheses and ensemble Kalman filter analyses, found that three of four tornadic supercells examined exhibited a secondary rear-flank gust front, commonly associated with internal outflow surges. Kosiba et al. (2013) used mobile Doppler radar data and mobile mesonet observations to conclude that genesis of the 5 June 2009 Goshen County, Wyoming, tornado was closely linked to a secondary rear-flank downdraft surge west of the pre-tornadic vortex. Skinner et al. (2014) used dual-Doppler radar, phased array radar, thermodynamic, and wind observations to identify four internal rear-flank downdraft surges in the 18 May 2010 Dumas, Texas, supercell. The downdrafts that produced the surges appeared to be forced dynamically when rotation was stronger near the surface than aloft. Skinner et al. (2015) used an ensemble Kalman filter analysis to further investigate these momentum surges and found that nonlinear dynamic perturbation pressure gradients near the surface drove the horizontal accelerations that produced the surges. Through a trajectory analysis, they found that air that entered the surges originated from near the surface on the north side of the mesocyclone and from inflow around 2 km above ground level (AGL). Marquis et al. (2016) assimilated ensemble Kalman filter analyses of the Goshen County, Wyoming, tornadic supercell into a high-resolution numerical model and found that tornadogenesis occurred when the air beneath the low-level mesocyclone was relatively warm and the surface circulation was strong and convergent.

There are also recent numerical studies that focus on the impacts of internal outflow surges. Beck and Weiss (2013) simulated a supercell and documented the forward-flank convergence boundary, formed by convergence of evaporatively cooled inflow and rain-free inflow, the left-flank convergence boundary, formed by convergence of evaporatively cooled inflow and evaporatively cooled downdraft air that descends from 2 to 3 km AGL, and the rear-flank gust front, which separates outflow in the rear flank of the storm from environmental air. They also found that ascent along these boundaries contributes to low-level vertical vorticity development through upward tilting of horizontal vorticity. The development of the left-flank convergence boundary could be the result of internal outflow surges. Their study demonstrates that the forward-flank region of supercells can be more complex than that suggested by the conceptual model of Lemon and Doswell (1979). Dahl et al. (2014) found that surface vertical vorticity in their simulated supercell forms owing to the vortex line slippage process described by Davies-Jones and Brooks (1993). The vertical vorticity is enhanced and organized into vertical vorticity "rivers" along internal storm boundaries, where surface convergence forces ascent and stretching (see their Fig. 5). Schenkman et al. (2016) investigated a tornado-triggering surge in a simulated supercell and found that air in the surge descends from around 2 km AGL. The descent is forced by a downward-directed vertical perturbation pressure gradient acceleration owing to a positive pressure perturbation that develops at the stagnation point between the mesocyclonic circulation and the environmental flow at 2–3 km. Descent is also forced by negative buoyancy and precipitation loading, especially in colder outflow surges. Riganti and Houston (2017) investigated the heterogeneity in the rear-flank outflow of the 10 June 2010 Last Chance, Colorado, supercell and hypothesized that it was related to Kelvin–Helmhotz instability behind the gust front.

Since outflow surges can produce near-surface convergence and generate vertical vorticity along their leading edges, the storm-relative locations of such surges may influence updraft intensity and tornado potential. Indeed, Markowski and Richardson (2017) found a large sensitivity between surface vortex development and the location of a heat sink in idealized "toy model" simulations of supercells. Outflow surges also feed the cold pool, the storm-relative location of which may impact whether outflow air can tilt or undercut the updraft, possibly decreasing storm longevity. The storm-relative location of outflow surges may impact the longevity of tornadoes by displacing them away from low-level mesocyclones (e.g., the Orleans, NE, tornado discussed by Marquis et al. 2012) or by tilting the updraft (Guarriello et al. 2018). Brown and Nowotarski (2019) found that a lower LCL height results in slower gust front propagation, presumably owing to a smaller density surplus within the outflow. Intense low-level rotation in their simulations resulted when the low- and midlevel mesocyclones were aligned with near-surface circulations in the outflow.

Most tornadoes and tornado fatalities are associated with supercell thunderstorms (Schoen and Ashley 2011; Anderson-Frey and Brooks 2019). Thus, better understanding environments that support long-lived supercells may aid in saving lives. There are relatively few case studies of long-lived supercells (e.g., Browning and Foote 1976; Glass and Britt 2002). A more thorough investigation by Bunkers et al. (2006) analyzed 224 long-lived supercells and found that most long-lived supercells are isolated, suggesting that storm mergers are generally detrimental to supercell longevity. They also found that long-lived supercells produced more F2–F5 tornadoes, stronger winds, and larger hail than short-lived supercells. They define a long-lived supercell as one that persists for more than 4 h and concluded that the demise of most long-lived supercells is simply owing to mesocyclone dissipation. Our investigation

of the impacts of the midlevel shear vector orientation on storm longevity using idealized numerical model simulations may lead to a better understanding of why some supercells persist longer than others.

The midlevel shear vector orientation, and thus the midlevel storm-relative winds, dictate where precipitation falls in a storm and where outflow surges may be more likely to occur, especially in the precipitation region. In this way, the orientation of the midlevel storm-relative winds may be another link between the environmental wind profile and the potential for long-lasting supercells and thus tornadoes. Furthermore, the midlevel shear vector orientation does not change many traditional supercell and tornado forecast parameters, including CAPE, CIN, low-level vertical wind shear, and the LCL height. Although the midlevel shear vector orientation can impact the magnitude of the deep-layer shear, storm motion, and thus SRH, it could still differ between two similar environments seemingly favorable for long-lived tornadic supercells and may not be captured by a traditional ingredients-based forecasting approach or composite parameters. For this reason, we choose to investigate how the backing or veering of the midlevel vertical wind shear vector may impact storm longevity, outflow surge location, and thus the potential for tornado-like vortex formation within simulated supercells. We give an overview of our methods in section 2, discuss results in section 3, and present conclusions in section 4.

2. Methods

We used CM1 (Bryan and Fritsch 2002), version 19.8, to perform idealized simulations of supercell thunderstorms. The model is initialized with the sounding launched at 1800 UTC 27 April 2011 at Jackson, Mississippi, during the largest documented outbreak of tornadoes in U.S. history (Knupp et al. 2014; Fig. 1). An isothermal layer was added between 1050 and 1150 m to suppress spurious convection in the model and only a single storm develops in all simulations. An idealized sickle-shaped hodograph is used for the vertical wind profile in our control (CNTL) simulation. Southerly winds increase from 0 to 20 kt (1 kt $\approx$ 0.51 m s^{-1}) in the lowest 0.5 km, the hodograph exhibits a quarter-circle turn from 0.5 to 1.0 km, and there is westerly shear from 1 to 6 km. Above 6 km, the winds are constant (solid hodograph in Fig. 1).

Our model domain size is 150 km $\times$ 150 km $\times$ 19.5 km with horizontal grid spacing of 250 m. The vertical grid spacing at the surface is 25 m, stretched to 325 m between 0.5 and 11.7 km, resulting in 108 vertical levels with 30 levels in the lowest 1 km. The time step is 0.5 s. We initialized convection using updraft nudging in the first 20 min of simulation time (Naylor and Gilmore 2012). The lateral boundary conditions are open-radiative, the upper and lower boundaries are free-slip, and a damping layer is included above 17 km. We employed the National Severe Storms Laboratory (NSSL) double-moment microphysical parameterization scheme with graupel and hail (Ziegler 1985; Mansell 2010; Mansell et al. 2010). The Coriolis force, surface fluxes, and radiation are neglected. Data are saved every minute and the simulations are terminated after 4 h.

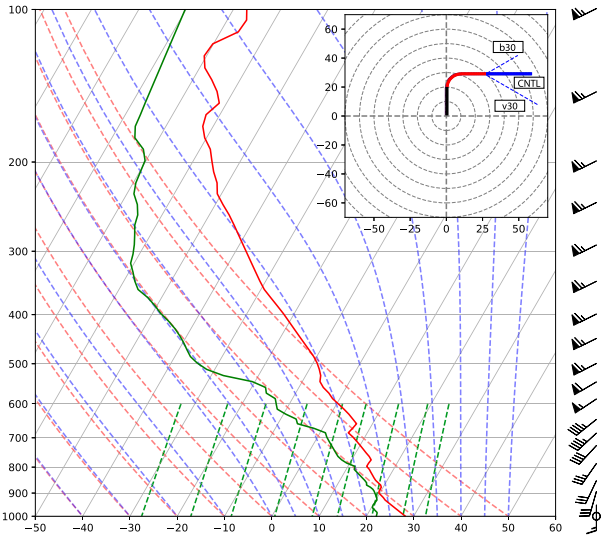

FIG. 1. Skew T–log$p$ diagram depicting the thermodynamic profile used to initialize all simulations. The solid hodograph (0–0.5 km: black; 0.5–3.0 km: red; 3.0–6.0 km: blue) was used to initialize the CNTL simulation. The dashed blue portions of the hodograph indicate the hodographs used to initialize the b30 and v30 simulations (labeled).

To obtain a range of midlevel shear vector orientations, we systematically altered the portion of the CNTL hodograph between 3 and 6 km (blue portion of the hodograph in Fig. 1) by veering and backing the shear vector by 10°, 20°, and 30°, yielding veering simulations named v10, v20, and v30 and backing simulations named b10, b20, and b30 (dotted hodographs labeled v30 and b30 in Fig. 1). The 0–6 km bulk shear remained 65 kt in all simulations.[1] Simulation initializations are identical otherwise. To obtain a larger ensemble, the v20, v30, b20, and b30 simulations were repeated twice with random wind perturbations applied to the hodograph at every level. Perturbations did not exceed ± 1 m s^{-1} ($\sim$1.94 kt; following Coffer et al. 2017). The same perturbations that were applied to the v20 hodograph were also applied to the b20 hodograph to obtain simulations named v20p1 and b20p1 for the first set of perturbations and v20p2 and b20p2 for the second set (and similarly for the v30 and b30 hodographs to produce v30p1, b30p1, v30p2, and b30p2). The v20, v30, b20, and b30 simulations were also repeated with the Morrison double-moment microphysical parameterization with hail (Morrison et al. 2005), yielding a suite of 19 simulations. While the idealized 0–3-km wind profile could also be altered, we held it constant to keep the number of simulations tractable and because of computational constraints. The relationship between variations in the wind profile and the storm motion described in

[1] We kept the 3–6-km bulk shear vector constant instead of the 0–6-km bulk shear vector in some preliminary simulations (not shown). In these simulations, as the 3–6-km shear vector became more backed, more 0–6-km bulk shear resulted, leading to an amplified signal in our results.

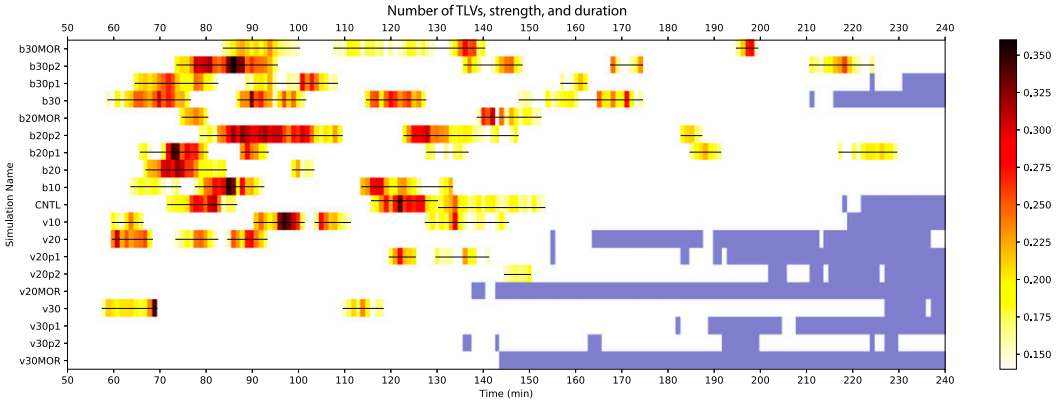

FIG. 2. Duration of individual TLVs (horizontal black lines; the CNTL simulation produces two separate TLVs that overlap at 130 min) and the maximum surface ζ within each TLV at times when the TLV criteria are met (shaded with warm colors; s^{-1}). Times when the maximum 2–5-km UH drops below 750 $m^2 s^{-2}$ are shaded blue.

Bunkers et al. (2000) is discussed in section 3a. Simulations with the shear vector veered are referred to as the veering simulations and those with the shear vector backed are referred to as the backing simulations.[2]

Massless flow tracers (hereafter "trajectories") were used to investigate properties of air that descends in the simulated supercell downdrafts. Both forward and backward trajectories are used and are calculated using a second-order semi-implicit discretization in space and time (section 2.1 of Miltenberger et al. 2013). The trajectory time step is the same as the output save interval (1 min). Only trajectories that remain above the lowest scalar model level are considered in any analyses herein as recommended by Vande Guchte and Dahl (2018). The initialization of trajectories is described in section 3c.

3. Results

a. *Tornado-like vortices and supercell longevity*

In each simulation, convection develops and becomes supercellular within the first hour. Most supercells produce tornado-like vortices (TLVs). Our TLV criteria are similar to those used by Coffer et al. (2017): vertical vorticity (ζ) at the surface exceeding 0.15 s^{-1},[3] a perturbation pressure deficit of at least 10 hPa over a depth of at least 1 km, and an instantaneous wind speed at the surface of at least 30 m s^{-1} for five or more time steps. Criteria-meeting time steps did not need to be consecutive, but a vortex was required to not drop below the thresholds for longer than four time steps (4 min) before regaining TLV strength. Stricter TLV criteria were tested and the results were qualitatively similar. Less-strict criteria resulted in too many spurious vortices classified as TLVs.

The supercells in the backing simulations produce more TLVs (average of 3.2 per simulation over the 4-h model integration) than those in the veering simulations (average of 1.3; Fig. 2). The TLVs are also longer lived in the backing simulations (11.9 min per TLV) than in the veering simulations (7.6 min per TLV). TLV strength, measured by surface ζ (Fig. 2), does not appear to be influenced by the midlevel shear vector orientation. Supercells in environments with the midlevel shear vector veered tend to dissipate earlier (defined by when the maximum 2–5-km updraft helicity, UH, drops below 750 $m^2 s^{-2}$, representative, for example, of an updraft exhibiting a mean vertical velocity of 15 m s^{-1} collocated with mean ζ of 0.017 s^{-1} in the 2–5-km layer; blue shading in Fig. 2)

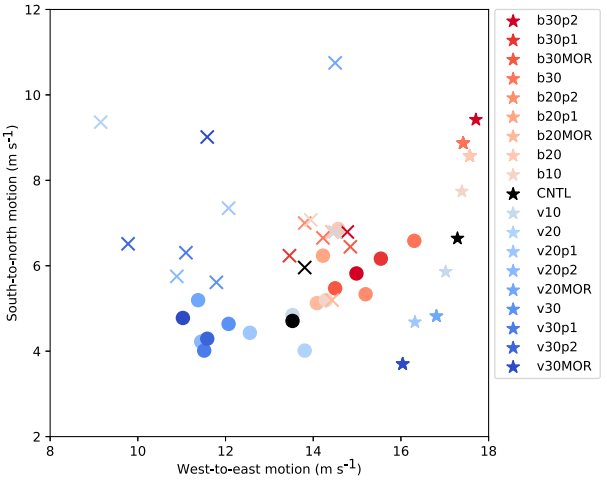

FIG. 3. Storm motion (m s^{-1}) calculated using the method described in Bunkers et al. (2000; stars) and average simulated storm motion for the second hour (circles) and third hour (crosses) for each simulation.

[2] Although we refer to the simulations with the 3–6-km shear vector backed as the "backing" simulations, the ground-relative (and storm-relative) winds never back with height in any of those simulations as in Parker (2017).

[3] Our ζ criterion is half that used in Coffer et al. (2017) because their horizontal grid spacing is 125 m and ours is 250 m.

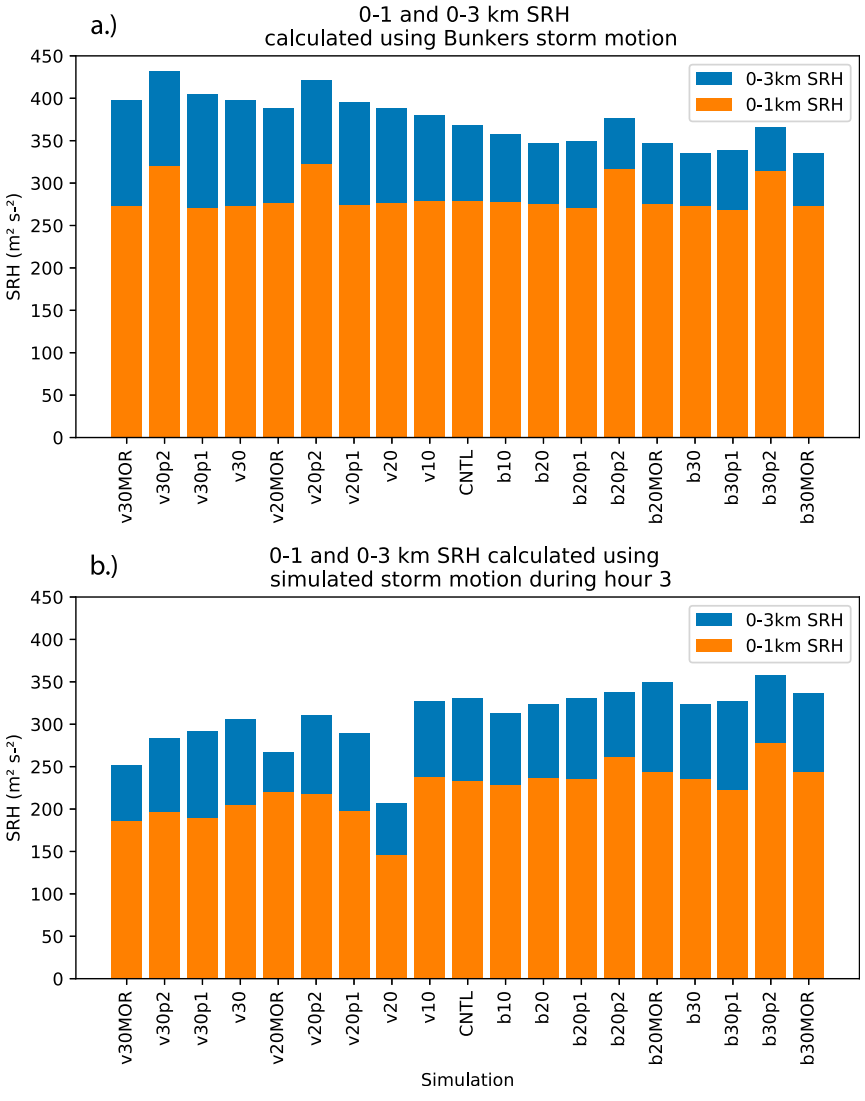

FIG. 4. The 0–1-km (orange) and 0–3-km SRH (blue; $m^2 s^{-2}$) for each simulation using the (a) storm motion described in Bunkers et al. (2000) and (b) average simulated storm motion during the third hour of each simulation.

while those in the backing simulations persist and may continue to produce TLVs over a longer period of time. Generally, the entire suite of simulations indicates that environments in which the midlevel shear vector is backed are more conducive to longer-lived supercells that can produce more and longer-lasting TLVs than are environments in which the midlevel shear vector is veered. This result is even more pronounced in the Morrison microphysics simulations (b30MOR, b20MOR, v20MOR, and v30MOR simulations; Fig. 2).

To explain this trend, we first investigated the SRH available to the supercells in all simulations. We found that, using storm motions calculated following Bunkers et al. (2000; Fig. 3), all supercells would experience similar 0–1-km SRH, but that the veering simulation environments exhibit greater 0–3-km SRH (Fig. 4a). Thus, one might expect the veering simulations to produce stronger and longer-lasting supercells owing to greater 0–3-km SRH, perhaps allowing for the production of more TLVs, but this is not consistent with our results. We recalculated the SRH using the simulated storm motion averaged over each hour. The motion of the simulated supercells differs from that calculated using the Bunkers method (Fig. 3). The Bunkers storm motions are too fast for all simulations and too far to the left of the simulated storm motions in the CNTL and backing simulations (Fig. 3). Simulated storm motions are similar for all simulations in the first hour, but differences emerge during the second hour of simulation time (Fig. 3), when the backing simulation supercells begin to move faster than those in the veering simulations. Furthermore, the backing simulation supercells generally maintain greater deviant rightward motion relative to the hodograph during the second and third hour of the simulations, while the veering simulation supercells generally begin turning left, yielding a storm motion closer to the hodograph

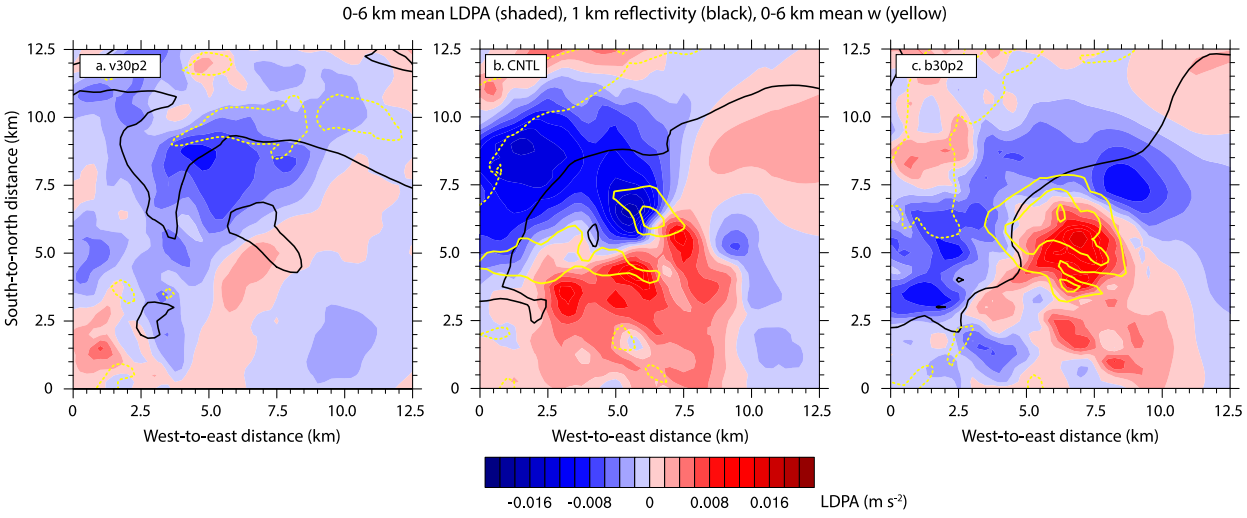

FIG. 5. The 0–6-km mean LDPA averaged between 120 and 150 min ($m\,s^{-2}$; shaded), 0–6-km vertical velocity (-2, 10, 15, and 20 $m\,s^{-1}$; yellow contours; negative values dashed, positive values solid), and 40-dBZ reflectivity contour at 1 km (black) at 150 min in the (a) v30p2, (b) CNTL, and (c) b30p2 simulations.

(Fig. 3). Thus, the backing simulation supercells generally experience greater 0–1- and 0–3-km SRH than those in the veering simulations with time (Fig. 4b). This is consistent with the results of Coniglio and Parker (2020), who found that more rightward storm motions contribute to greater SRH owing to stronger storm-relative flow. Peters et al. (2020) also found that stronger storm-relative winds contribute to stronger updrafts, as discussed below.

The backing simulation supercells maintain greater deviant rightward motion owing to a more persistent upward-directed linear dynamic perturbation pressure gradient acceleration (LDPA; Rotunno and Klemp 1982). The LDPA is proportional to the vertical derivative of the dot product of the environmental vertical wind shear vector and the horizontal gradient in vertical velocity [LDPA $\propto (\partial/\partial z)(\mathbf{S}\cdot\nabla_h w)$, where $\mathbf{S}$ is the vertical wind shear vector]. Although the orientation of the 3–6 km shear vector changes between simulations, the 0–6-km bulk shear magnitude is constant across all simulations. The horizontal vertical velocity gradient, however, depends greatly on the magnitude of an updraft. The updrafts in the backing simulations are stronger and persist longer, meaning that the magnitude of the vertical velocity gradient is greater in the backing simulations, particularly during the second and third hours, leading to a stronger and longer-lasting LDPA on the right flank of those storms and thus more deviant rightward motion and stronger storm-relative flow and SRH (Figs. 5 and 6).

Trapp et al. (2017) explored theoretical calculations and idealized simulations and concluded that larger mesocyclones should more readily produce larger and stronger tornadoes, provided that there is a source of near-surface ζ. Although we did not find a relationship between TLV strength and the midlevel shear vector orientation, we did find that TLVs last longer in the backing simulations. Perhaps TLV production and maintenance is related to mesocyclone size since larger mesocyclones promote better alignment or overlap of upward dynamic accelerations with near-surface rotation (e.g., Guarriello et al. 2018; Brown and Nowotarski 2019). Using the number of grid points with 2–5-km UH greater than 750 $m^2\,s^{-2}$ as a proxy for mesocyclone size, backing simulation supercells obtain and maintain larger mesocyclones (Fig. 7) than those in the veering simulations. The veering simulation mesocyclones become larger more rapidly, but these early simulation times (0–30 min) are likely unrepresentative of the real atmosphere because we use artificial updraft nudging during the first 20 min of the simulations. All simulated mesocyclones achieve a similar size after a dominant updraft becomes established by 40 min, when updraft nudging has been off for 20 min. The mesocyclone size peaks around 40–60 min (most backing simulations peak later, around 60 min), roughly 10–20 min before most simulated supercells produce their first TLV (Fig. 2). Afterward, the mesocyclones become smaller, although they generally remain larger in the backing simulations. Updraft strength and mesocyclone size differences between the veering and backing

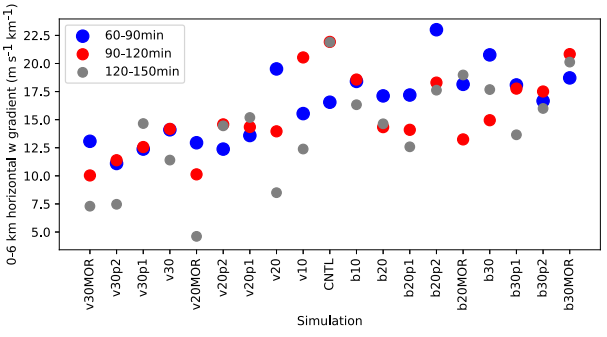

FIG. 6. Maximum $\nabla_h w$ ($m\,s^{-1}\,km^{-1}$) averaged over the 0–6-km layer in a 25 km × 25 km box centered on the 2–5-km updraft maximum averaged between 60 and 90 min (blue), 90 and 120 min (red), and 120 and 150 min (gray) in each simulation.

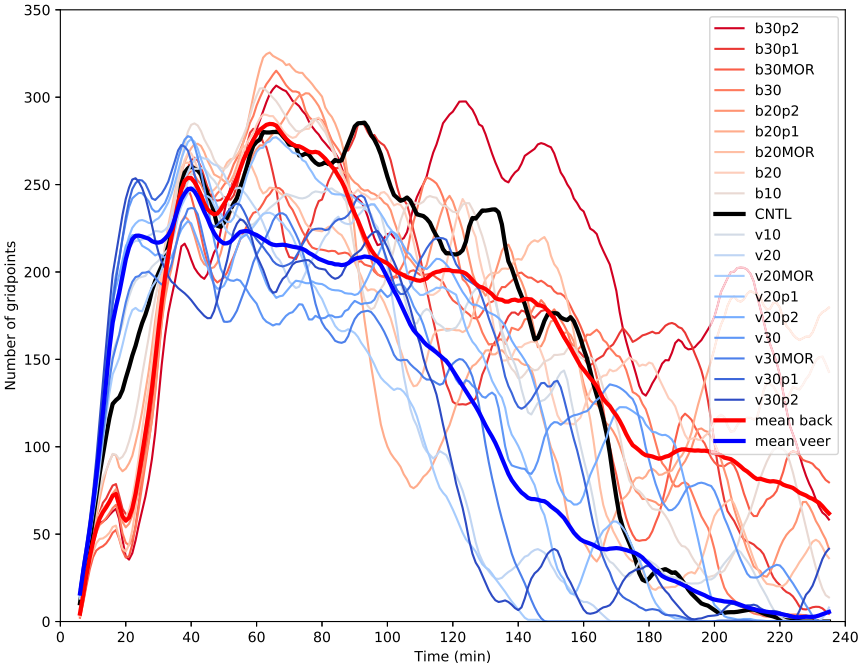

FIG. 7. The 10-min rolling average (centered on analysis time) of the number of grid points with 2–5-km UH $> 750\,m^2\,s^{-2}$ in each simulation. Thick lines are averages of all veering (blue) and backing (red) simulations. The thick black line is the 10-min rolling average of the CNTL. Only a single storm develops in all simulations.

simulations begin around 50 min because the simulated supercells produce the first outflow surges (defined in section 3b) around 30–40 min and there is a lag time of at least 15 min (discussed in section 3d) before an outflow surge can dramatically influence updraft intensity.

Updrafts exhibit larger $\nabla_h w$ in the backing simulations (Figs. 5c and 6) and thus greater upward-directed LDPA exists on the right flank of those supercells, yielding more deviant rightward motion and thus more SRH, favoring stronger mesocyclones. Since larger and stronger mesocyclones are maintained for longer in the backing simulations, there are also more persistent and stronger upward-directed nonlinear dynamic perturbation pressure gradient accelerations [NDPA $\propto (\partial/\partial z)(\zeta^2)$; not shown], which aid in stretching of near-surface ζ into TLVs (e.g., Orf et al. 2017) for a longer period of time. Updrafts and mesocyclones are smaller and weaken earlier in the veering simulations, yielding weaker LDPA, less deviant rightward motion, and less SRH, favoring weaker mesocyclones, weaker NDPA, and less potential for stretching of near-surface ζ into TLVs later in these simulations.

b. *Outflow surge characteristics*

Another striking difference between the simulations is the location of outflow surges within the simulated supercells. Outflow surges are defined if there is surface divergence $\geq 0.02\,s^{-1}$, a surface density potential temperature perturbation $(\theta'_\rho) \leq -4$ K, vertical velocity $(w) \leq -6\,m\,s^{-1}$ at 500 m, and 1-km reflectivity ≥ 40 dBZ. If multiple adjacent surface grid points meet these criteria, then the point exhibiting the maximum divergence is taken to be the center of the surge.[4] We tested other thresholds when developing these criteria, and found that the $\theta'_\rho < -4$ K criterion was best at discriminating between outflow air in general and stronger internal surges of outflow. The w and divergence criteria aid in finding the center of an outflow surge. We added the 1-km reflectivity criterion to ensure that only outflow surges in the precipitation regions of storms are considered. Output was subjectively analyzed to group times when the criteria were met into continuous outflow surges. Outflow surges were required to meet all criteria for at least three consecutive time steps and be spatially contiguous.

We selected a subset of simulations (v30p2, v20p2, v20, CNTL, b20, b20p2, and b30p2) for further analysis of outflow surges. These simulations were selected because they best represent the trend that backing simulation supercells persist longer and produce more TLVs while veering simulation supercells dissipate earlier and produce fewer TLVs (Fig. 2). Outflow surges in the backing simulations generally occur more northwest of the 2–5-km updraft maximum, whereas outflow surges in the veering simulations occur more north or northeast of the updraft maximum (Figs. 8–10). Outflow surges

[4] If multiple surges are occurring at the same time, then the algorithm described above is used to identify one surge and the center of any other surge was chosen to be the center of any separate regions meeting the outflow surge criteria.

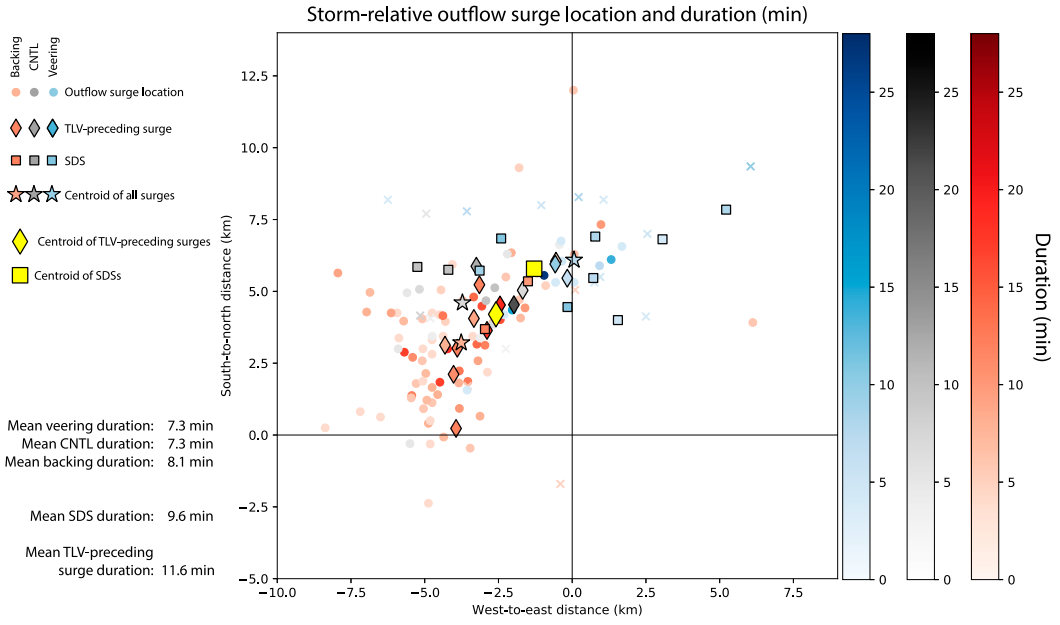

FIG. 8. The 2–5-km updraft-relative location of outflow surges (dots), TLV-preceding surges (diamonds), SDSs (squares), and outflow surges that occur after the first SDS (crosses) in the backing (red), CNTL (gray), and the veering (blue) simulations from the subset discussed in the text, and the centroids of all surges in each set of simulations (stars), of all TLV-preceding surges (yellow diamond), and of all SDSs (yellow square). The shading of all symbols (except the yellow diamond and square) represents the duration (min) of an outflow surge. The mean duration of all backing, CNTL, veering, storm-dissipating, and TLV-preceding surges in the subset of simulations are provided at the lower left.

in the CNTL simulation generally occur between those in the backing and veering simulations.

Outflow surges from the subset were subjectively analyzed to determine if there is a specific outflow surge that contributes to the demise of a supercell [storm-dissipating surge (SDS)]. An outflow surge was deemed an SDS if the outflow surge air passed beneath and away from an updraft such that the updraft either began a dramatic weakening trend and/or dissipated soon afterward. As an outflow surge passes beneath an updraft, the updraft often becomes tilted (discussed in section 3d). Some simulations exhibit multiple SDSs, with each one yielding outflow air that tilts the low-level updraft, weakening, and ultimately undercutting it. For simulations in which multiple SDSs were identified, it is likely that without multiple surges in succession, the storm may not have dissipated. For example, the updraft could have recovered after the first surge, or the later surges alone would have been too weak to tilt, weaken, and undercut the updraft without the first, stronger surge. When possible, we identified one single surge responsible for storm demise.

The SDSs tend to occur more to the north of the 2–5-km updraft maximum (squares in Figs. 8–10), where outflow surges are more common in the veering simulations. Outflow surges that precede TLVs occur in more variable updraft-relative locations (diamonds in Figs. 8–10), but the centroid is more northwest of the updraft (yellow diamond in Figs. 8–10). TLV-preceding surges tend to last longer (mean duration of 11.6 min) than SDSs (mean duration of 9.6 min; Fig. 8 and Table 1). Initially, we expected SDSs to exhibit a longer duration than TLV-preceding surges because a longer outflow surge duration should yield more negatively buoyant air, but we found that the opposite occurred in our simulations. Since the storm-relative location of outflow surges varies systematically across the simulations, and that TLV-preceding surges last longer than SDSs, this suggests that the storm-relative location of outflow surges impacts supercell longevity more than outflow surge duration (Fig. 8). Furthermore, the mean duration of outflow surges in the veering simulations and the CNTL simulation was the same (7.3 min) and only slightly longer in the backing simulations (8.1 min; Fig. 8 and Table 1), again suggesting that storm demise is not caused by longer-lasting outflow surges.

We also investigated how many grid points exhibited 2–5-km UH $> 750\,m^2\,s^{-2}$ at the time of outflow surges, with more grid points indicating a larger and/or stronger mesocyclone and updraft. The number of grid points with 2–5-km UH $> 750\,m^2\,s^{-2}$ is generally greater during outflow surges in the backing simulations (mean of 194) and the CNTL simulation (mean of 210) and less in the veering simulations (mean of 147; Fig. 9 and Table 1). This is likely a result of the veering simulation supercell updrafts and mesocyclones weakening earlier (Figs. 2 and 7). The mean number of grid points with 2–5-km UH $> 750\,m^2\,s^{-2}$ during TLV-preceding surges is 236 while it is only 122 during SDSs (Fig. 9 and Table 1), likely because larger mesocyclones produce larger areas of upward-directed NDPA, making stretching of surface ζ into a TLV more likely (Trapp

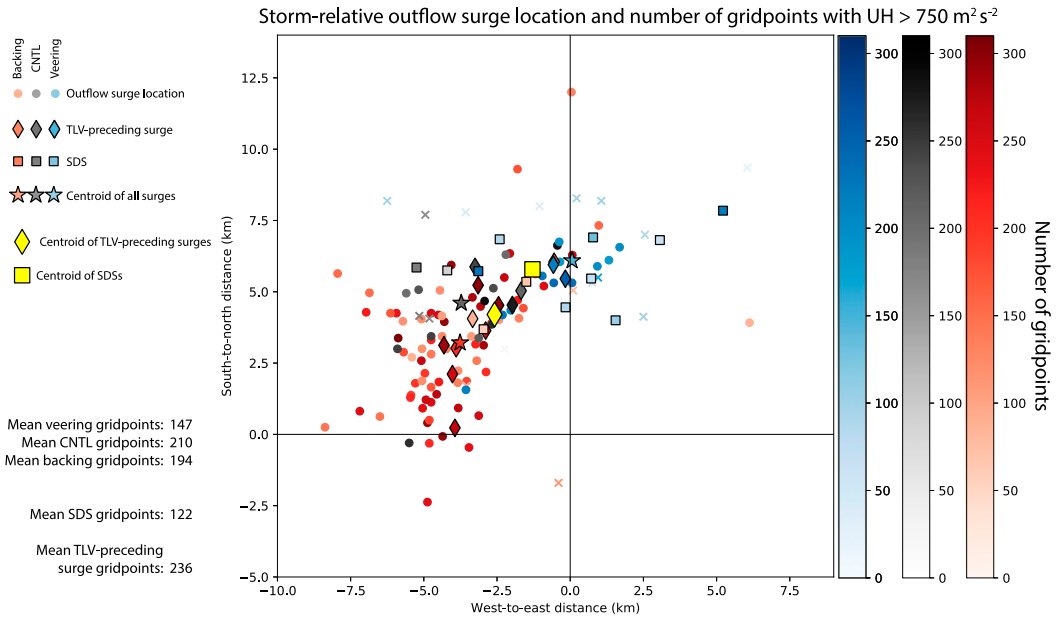

FIG. 9. As in Fig. 8, but the shading of all symbols represents the number of grid points exhibiting UH > 750 $m^2 s^{-2}$ averaged during the corresponding outflow surge. The mean number of grid points for all backing, CNTL, veering, storm-dissipating, and TLV-preceding surges in the subset of simulations are provided at the lower left.

et al. 2017). Smaller or weaker mesocyclones produce weaker upward-directed NDPA and are likely more susceptible to being undercut by outflow. This result also reflects that SDSs are more common in the veering simulations, which also exhibit smaller and/or weaker mesocyclones.

We additionally investigated θ'_ρ at the centers of outflow surges and found little variation between simulations, with mean values of −5.7 K in the veering simulations, −6.3 K in the CNTL, and −5.9 K in the backing simulations (Fig. 10; Table 1). There was also little difference between the mean θ'_ρ values of TLV-preceding surges (−6.2 K) and SDSs (−6.9 K; Table 1). The mean θ'_ρ values are taken at the center of each surge and are not necessarily representative of the outflow air as it flows away from the area of descent. Thus, in our simulations, early storm dissipation is not attributable to colder outflow surges, again suggesting that the storm-relative location of outflow surges is the most important factor in early storm demise.

The variation in outflow surge location is largely explained by where the greatest precipitation loading occurs between 1 and 3 km, which is the source of most of the outflow surge air (discussed in section 3c). We define precipitation loading as the total mixing ratio of rain, snow, graupel, and hail. The midlevel shear vector orientation (i.e., the mid- and upper-level storm-relative winds) strongly impacts where hydrometeors are transported within and fall out of a storm, leading to differences in the location of outflow surges (Fig. 11). When the midlevel shear vector is veered, more precipitation falls in the forward flank of a storm, meaning that outflow surges are more prevalent north or northeast of the 2–5-km updraft maximum (Figs. 8–10). When the midlevel shear vector is backed, more precipitation falls in the left and rear flanks of a storm, consistent with outflow surges more prevalent northwest or west of the 2–5-km updraft maximum in the backing simulations (Figs. 8–10). This result is consistent with that found in Warren et al. (2017). The variation in storm-relative outflow surge location between simulations may impact baroclinic vorticity generation as outflow air flows toward an updraft, an investigation of which is left for future work.

We speculate that our results are Galilean invariant, especially since friction is not included in the simulations. Since most precipitation forms above 3 km, we do not expect *large* changes in the updraft-relative outflow surge location when using different low-level (0–3-km) hodographs. Weaker low-level shear would likely result in shorter-lived storms in all simulations, and thus less obvious differences in storm longevity and TLV formation. Stronger low-level shear would likely make the results more obvious, as in our second set of perturbation simulations (v30p2, v20p2, b20p2, and b30p2; Fig. 2).

c. *Trajectory analysis*

We initialized forward and backward trajectories within outflow surges to investigate θ'_ρ of the outflow air passing beneath updrafts and the net downward excursion of trajectories that enter outflow surges. Trajectories are initialized in 3 km × 3 km × 2 km boxes centered on select SDSs and TLV-preceding surges. Trajectories are initialized every 250 m in the horizontal and at every model level within the lowest 2 km, providing a total of 6929 total trajectories per surge. Forward trajectories are integrated for 10 min and backward

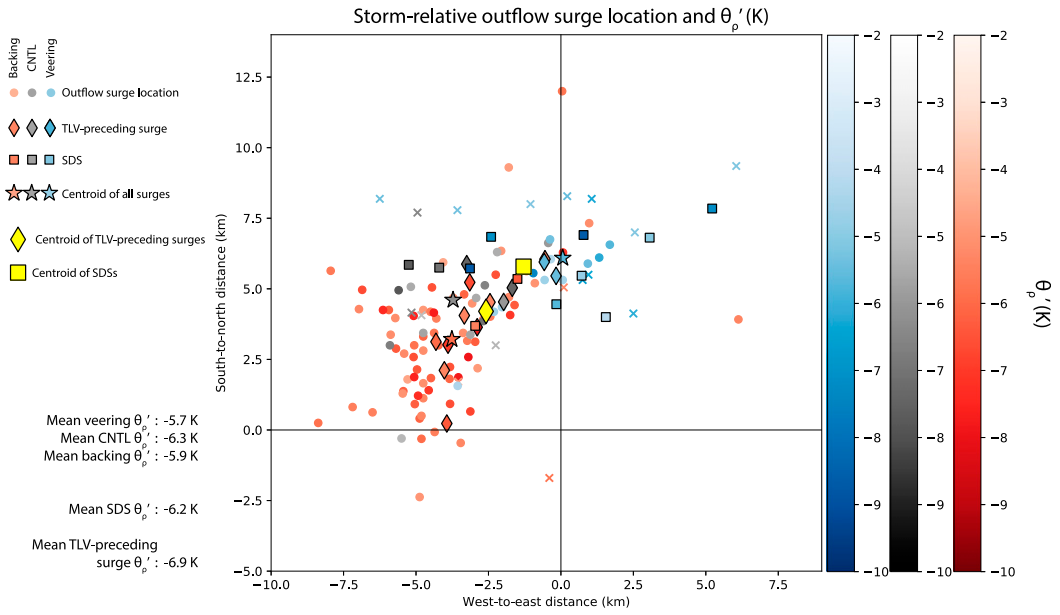

FIG. 10. As in Fig. 8, but the shading of all symbols represents the mean θ'_ρ (K) at the center of the corresponding outflow surge. The mean values of θ'_ρ for all backing, CNTL, veering, storm-dissipating, and TLV-preceding surges in the subset of simulations are provided at the lower left.

trajectories are integrated for 20 min. Trajectories initialized in the surge that precedes the first TLV in the CNTL simulation are shown in Fig. 12. Trajectories generally approach a downdraft from the east or southeast, descend, move southward near the surface, and then either are ingested by or pass beneath the updraft. Values of streamwise vorticity approach 0.1 s^{-1} when trajectories are near the surface (brown shading in Fig. 12a), likely owing to horizontal stretching as parcels accelerate away from a downdraft and toward an updraft. These large values of streamwise vorticity exist in all simulations and for most outflow surges, similar to previous studies. Marquis et al. (2016) found horizontal vorticity values of 0.06–0.08 s^{-1} along parcel trajectories within the forward-flank baroclinic zone in the Goshen County, Wyoming, tornadic supercell. Orf et al. (2017) identified a streamwise vorticity current (SVC) in their high-resolution simulation of a long-tracked tornadic supercell. They found that the SVC is tilted by the updraft and that the intensification of the SVC precedes tornadogenesis. Finley et al. (2018) also documented an SVC in their high-resolution simulation of a tornadic supercell on 27 April 2011. We leave an investigation of the origins of this streamwise vorticity current in our simulations for future work.

We used the forward trajectories to investigate the buoyancy of the outflow surge air that passes beneath the 1 km updrafts (defined by $w > 15\ m\ s^{-1}$; i.e., we only considered trajectories that pass beneath grid points exhibiting 1-km $w > 15\ m\ s^{-1}$ somewhere along the trajectory). The values of θ'_ρ along these forward trajectories are only calculated while a trajectory remains below 1 km. For these trajectories, the mean θ'_ρ of TLV-preceding surges is −2.4 K and the mean θ'_ρ of SDSs is −1.7 K (Fig. 13 and Table 2), again suggesting that the buoyancy of outflow surge air is not a determining factor between TLV formation or storm dissipation in a given thermodynamic environment, provided that the outflow surge air is not too cold to be ingested by an updraft (e.g., Markowski et al. 2002). There is not a significant difference in the mean θ'_ρ of the air that passes beneath the updrafts between the veering (−1.6 K) and backing simulations (−2.3 K; Fig. 13 and Table 2) either, which is not surprising since all simulations are initialized with the same thermodynamic profile.

TABLE 1. Mean duration (min) of outflow surges, mean number of grid points exhibiting UH > 750 $m^2\ s^{-2}$ during outflow surges, and mean θ'_ρ (K) at the center of outflow surges in the veering, CNTL, and backing simulations as well as for SDSs and TLV-preceding surges.

	Mean duration (min)	Mean number of grid points with UH > 750 $m^2\ s^{-2}$	Mean θ'_ρ (K)
Veering simulations	7.3	147	−5.7
CNTL simulation	7.3	210	−6.3
Backing simulations	8.1	194	−5.9
SDSs	9.6	122	−6.9
TLV-preceding surges	11.6	236	−6.2

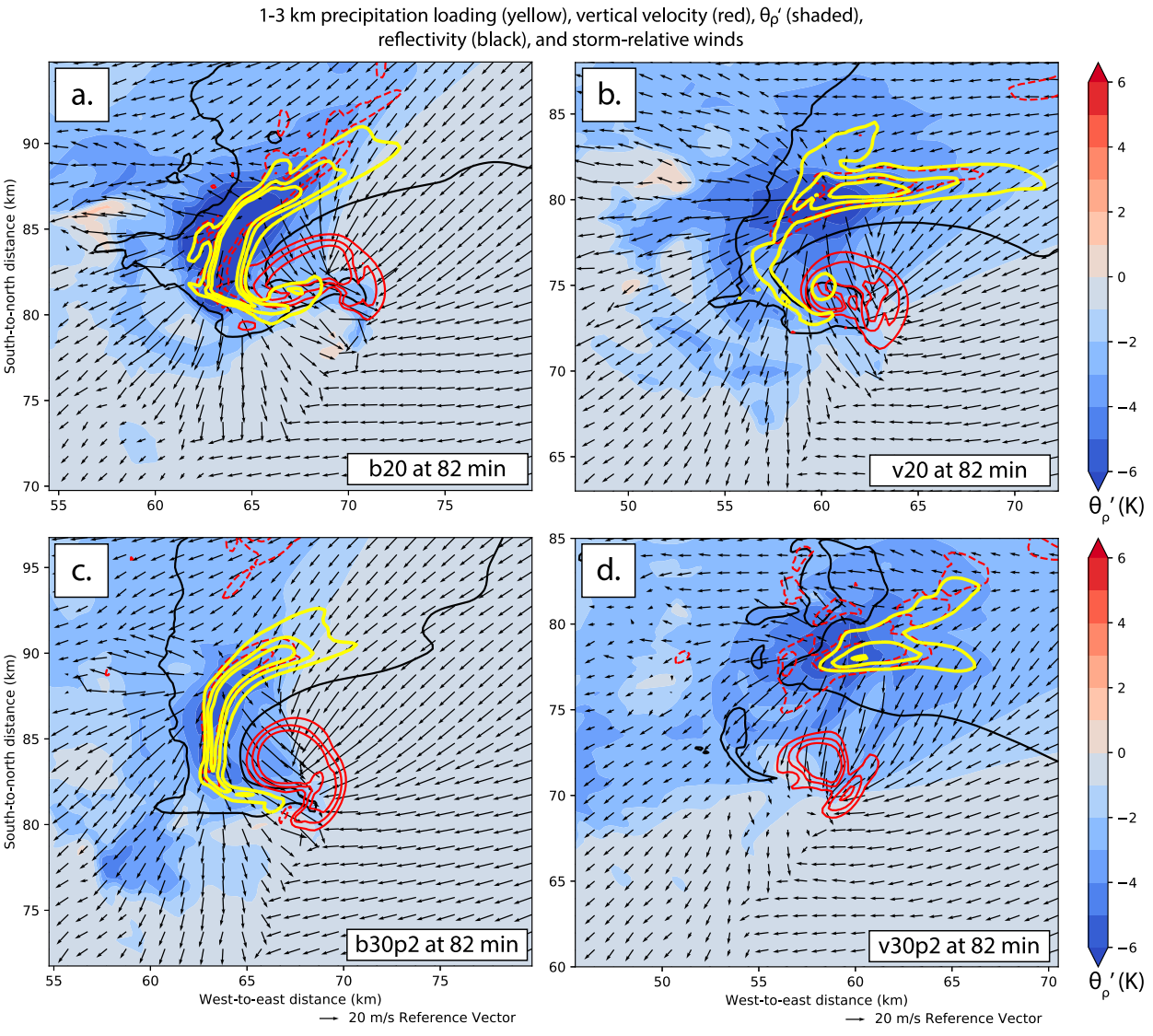

FIG. 11. Surface θ'_ρ (K; shaded), 1–3-km vertical velocity (−8, −4, 10, 15, 20 m s^{-1}; red contours; negative values dashed and positive values solid), 1–3-km precipitation loading (0.05, 0.10, and 0.15 kg kg^{-1}; yellow contours; see text for definition), 40-dBZ reflectivity contour at 1 km (black), and surface storm-relative winds (arrows) in the (a) b20, (b) v20, (c) b30p2, and (d) v30p2 simulations at 82 min.

Backward trajectories were used to investigate the mean net downward excursion (defined as the difference between the maximum and initialization heights of a backward trajectory) of the outflow air that passes beneath a 1 km updraft. There is no significant difference in mean net downward excursion between the veering (1034 m) and backing (1233 m) simulations or between SDSs (1093 m) and TLV-preceding surges (1245 m; Fig. 14 and Table 2). Generally, the net downward excursion of outflow surge trajectories is between 0.5 and 2.0 km (consistent with Beck and Weiss 2013 and Schenkman et al. 2016), but may be as high as about 5 km.

d. Impacts of the storm-relative outflow surge location

The variation in outflow surge location likely explains why the veering simulation supercells dissipate earlier while the backing simulation supercells persist longer. When outflow surges occur northwest of an updraft, outflow air is wrapped into the rear flank of a storm in the hook-echo region (Figs. 11a,c), permitting unmodified inflow east and southeast of and strong convergence to develop beneath an updraft. When outflow surges occur north or especially northeast of an updraft, however, negatively buoyant air becomes more widespread in the inflow region east of a storm (Figs. 11b,d) and less convergence results beneath an updraft (discussed later in this section). Time–height plots of the maximum updraft strength in the subset of simulations indicate that SDSs precede or coincide with a weakening of updrafts from the bottom upward (Figs. 15a–d,f). Some simulations exhibit multiple SDSs, each of which further tilt and weaken the updraft, leading to storm dissipation (Figs. 15a–d,f). In the

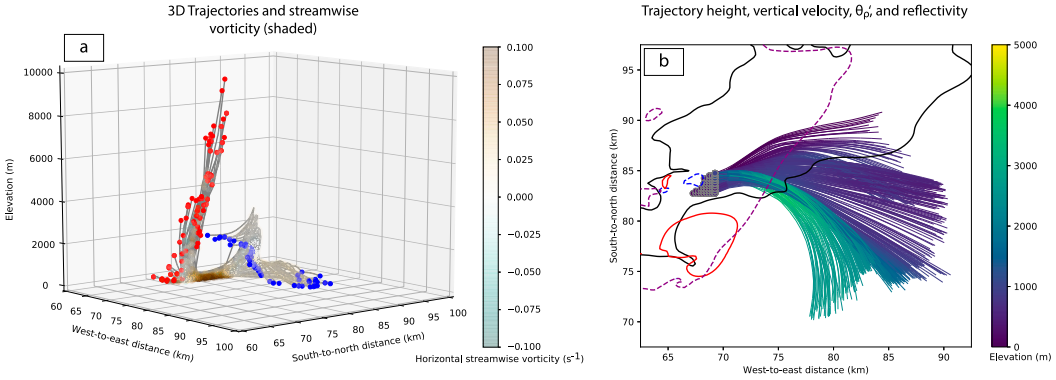

FIG. 12. (a) Three-dimensional depiction of trajectories (gray lines; both back and forward trajectories joined together) within the outflow surge that precedes the first TLV in the CNTL simulation as viewed from the southeast. Starting points of the back trajectories are blue, ending points of the forward trajectories are red, and horizontal streamwise vorticity (s^{-1}) is shaded along each trajectory. (b) The back trajectories in (a) projected onto the x–y plane with trajectory height (m) shaded, 40-dBZ reflectivity contour at 1 km (black), −1-K θ_ρ' contour at the surface (dashed purple), 10 m s^{-1} w contour at 3 km (red), and −8 m s^{-1} w contour at 250 m (dashed blue) at the beginning of the TLV-preceding surge (57 min) in the CNTL simulation.

b30p2 and b20 simulations, there were no analyzed SDSs and the updrafts remain strong (generally >25 m s^{-1} in the lowest 3 km; Figs. 15e,g).

SDSs also precede or coincide with an increase in the separation distance (e.g., Guarriello et al. 2018) between the 1 and the 3–6-km updraft maxima (a proxy for updraft tilt; Figs. 16a–d,f), suggesting that as an SDS approaches an updraft from the north, the low-level updraft is displaced southward from the midlevel updraft, leading to a tilted updraft and potential storm dissipation, as explained below. In simulations without SDSs, the updrafts do not tilt much with height (Figs. 16e,g). The lag time between an outflow surge reaching the surface and maximum updraft tilt is at least 15 min. For example, the first SDS in the CNTL simulation (Fig. 16a) occurs at 137 min and the updraft tilt reaches a relative maximum around 152 min.

Another example of an SDS leading to significant updraft tilt exists in the v30p2 simulation. An SDS occurs north of the updraft at 98 min (Fig. 17a, consistent with Figs. 8–10), while the updraft is upright, ζ values exceed 0.025 s^{-1} in the 2–5-km layer, and the upward-directed perturbation pressure gradient ($\partial p'/\partial z$) exceeds −1.5 hPa km^{-1} at 1 km and −1.0 hPa km^{-1} at 500 m (Fig. 17b). At 106 min, the outflow surge passes beneath the updraft and much of the air in the surge continues southward and is not ingested by the updraft (Figs. 17c,d). The updraft is still rotating ($\zeta \geq 0.015$ s^{-1} at 3 km), but has weakened (from 22 to 15 m s^{-1} at 3 km) and become tilted (2-km distance between the 1- and 3-km updraft maxima). The low-level upward-directed $\partial p'/\partial z$ has also shifted southward with the leading edge of the surge and weakened (Figs. 17c,d). By 118 min, the updraft tilt has become large (roughly 4 km between the 1-km updraft and 3-km updraft maxima; Figs. 17e,f) and there is no concentrated

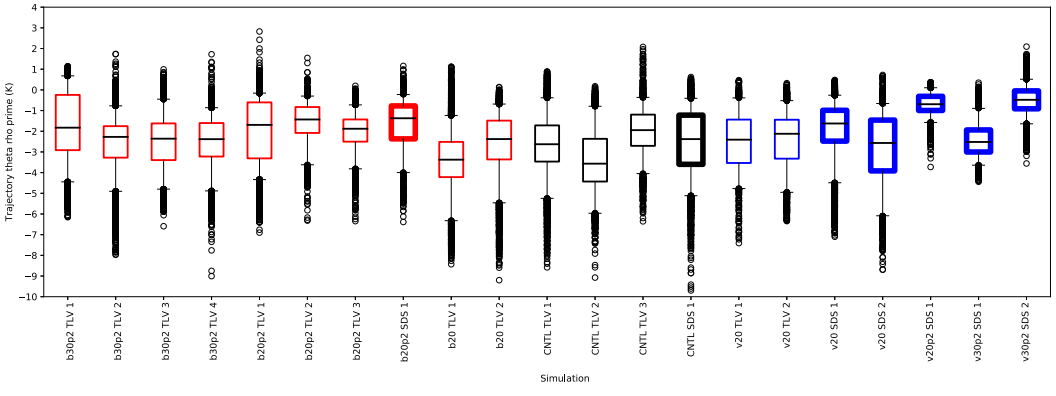

FIG. 13. Box-and-whisker plots of θ_ρ' along all forward trajectories that pass beneath the 1-km updraft (defined by the 15 m s^{-1} updraft contour) for selected TLV-preceding surges (thin boxes) and SDSs (bold boxes) in the subset of backing (red), CNTL (black), and veering (blue) simulations. The horizontal lines within each box represent the median, the boxes extend to the lower and upper quartiles, and the whiskers extend to the 5th and 95th percentiles. Circles are outliers.

TABLE 2. Mean θ_ρ' (K) and net downward excursion (m) of trajectories initialized in select outflow surges. Values of θ_ρ' are only calculated along forward trajectories that pass beneath a 1-km updraft of at least 15 m s^{-1} and while a trajectory is below 1 km.

	Mean θ_ρ' (K)	Mean net downward excursion (m)
All selected surges	−2.2	1211
Veering simulations	−1.6	1034
CNTL simulation	−2.6	1372
Backing simulations	−2.3	1233
SDSs	−1.7	1093
TLV-preceding surges	−2.4	1245

area of upward-directed $\partial p'/\partial z$ beneath the midlevel updraft to force air to its level of free convection (Fig. 17f). Convergence decreases beneath the 2–5-km updraft throughout this period as the surface winds beneath the updraft become northeasterly (Figs. 17a,c,e). After this time, the updraft and supercell continue to dissipate.

Most outflow surges do not result in storm demise, and some may lead to TLV formation (e.g., Fig. 18). An outflow surge occurs northwest of the updraft in the b20p2 simulation at 106 min (Fig. 18a; consistent with Figs. 8–10). At this time, the updraft is upright, ζ exceeds 0.020 s^{-1} in the 2–5-km layer, and there is a concentrated area of upward-directed $\partial p'/\partial z$ beneath the updraft (−2.0 hPa km^{-1} at 1 km and 500 m; Fig. 18b). As the outflow surge passes beneath the updraft at 112 min, the updraft weakens slightly (from 18 to 16 m s^{-1} at 3 km) and acquires a slight northwestward tilt with height over the outflow. Rotation is maintained in the updraft and upward-directed $\partial p'/\partial z$ is maintained near the surface within the area of convergence along the outflow surge boundary, which does not surge away from the updraft, particularly on the eastern side of the updraft (Figs. 18c,d). By 120 min, the updraft has reintensified to 20 m s^{-1} at 3 km and again become upright with $\zeta > 0.015$ s^{-1} at 1 km and a concentrated area of upward-directed $\partial p'/\partial z$ beneath it (Figs. 18e,f). Convergence beneath the 2–5-km updraft remains greater than that in the v30p2 example as northeasterly inflow converges with westerly outflow throughout this period (cf. Figs. 17a,c,e and 18a,c,e; mean convergence values are discussed further below). A TLV occurs in this simulation shortly after this time at 123 min (Fig. 2).

Outflow surges that result in severe low-level updraft tilt are likely detrimental to a storm because any low-level upward-directed $\partial p'/\partial z$ becomes separated from the midlevel mesocyclone and associated NDPA. Without low-level upward-directed $\partial p'/\partial z$, it is unlikely that even slightly negatively buoyant outflow air will be able to rise to its level of free convection. If the updraft tilt does not become too large, however, then a storm may recover from a surge owing to increased convergence beneath the updraft (e.g., Brown and Nowotarski 2019), as discussed below.

Assuming that almost all surface-based supercells produce ζ near the ground (e.g., Rotunno and Klemp 1985; Davies-Jones and Brooks 1993; Dahl 2015), then an important factor in storm longevity and TLV production is whether convergence can be maintained beneath an updraft. Near-surface convergence aids in both maintaining low-level updrafts by forcing near-surface ascent and concentrating surface ζ to be stretched by the low-level updraft, possibly into a TLV (e.g., near-surface vortices merging into a pre-tornadic vortex owing to surface convergence and eventually forming a tornado as documented by Schenkman et al. 2014). The backing simulations produce more convergence near the surface beneath the 2–5-km updraft maxima over a longer duration than do the veering simulations (Fig. 19) owing to outflow surges northwest of the updrafts providing more westerly outflow winds. The mean veering simulation convergence drops below 0.005 s^{-1} within the first hour and approaches zero after 160 min, while the mean backing simulation surface convergence is at least 0.005 s^{-1} through about 160 min and remains convergent until the last few minutes of the model integration (convergence is negative divergence; Fig. 19). These averages only include simulations that exhibit a supercell with 2–5-km UH > 750 m^2 s^{-2} at a given time.

The tendency for outflow surges to occur more north or northeast of updrafts in the veering simulations at least partially explains why there is less surface convergence beneath

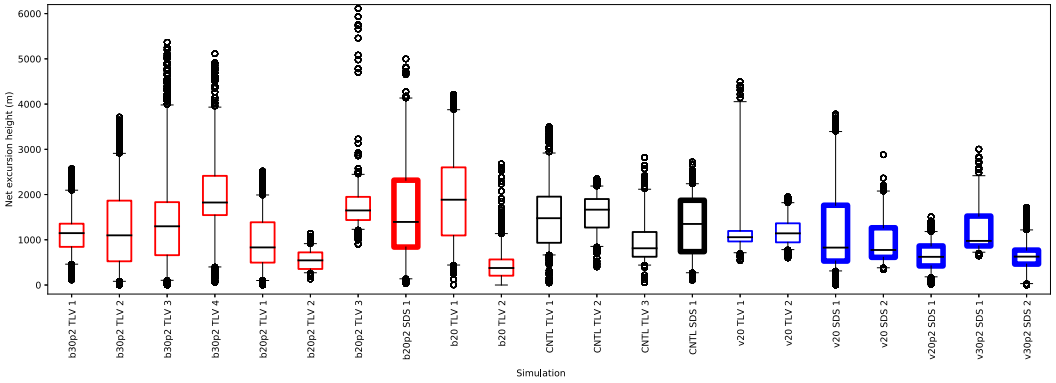

FIG. 14. As in Fig. 13, but for the net downward excursion in the 20 min prior to trajectory initialization of trajectories that pass beneath the 1-km updraft.

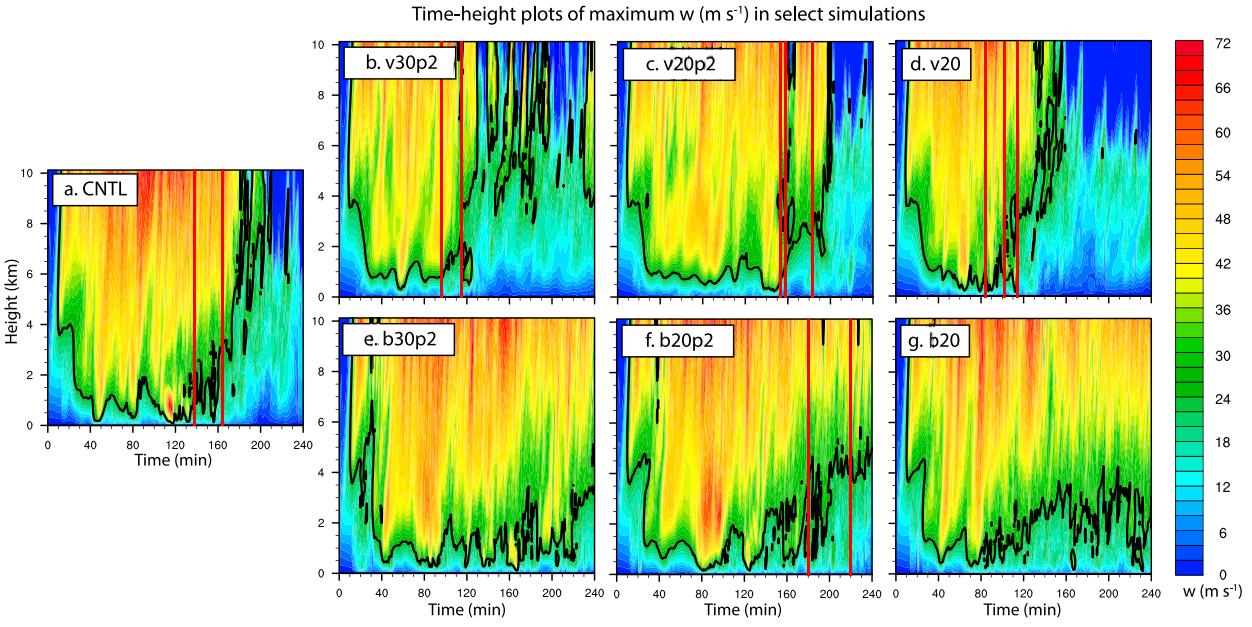

FIG. 15. Time–height plots of maximum updraft (m s^{-1}; shaded, black line is the 25 m s^{-1} contour) in the (a) CNTL, (b) v30p2, (c) v20p2, (d) v20, (e) b30p2, (f) b20p2, and (g) b20 simulations. Vertical red lines indicate times of SDSs.

the updrafts in those simulations. Figure 17a depicts northeasterly storm-relative winds emanating from an outflow surge in the v30p2 simulation. The ambient storm-relative winds are also northeasterly or easterly and the storm-relative winds behind the rear-flank gust front are northerly, producing relatively weak surface convergence beneath the 2–5-km updraft maximum. In the b20p2 simulation (Fig. 18a), the storm-relative winds in the outflow surge approach the updraft from the northwest while the ambient storm-relative winds are northeasterly and the storm-relative winds behind the rear-flank gust front are westerly, producing greater convergence beneath the updraft and along the outflow boundaries. The storm-relative inflow in the veering simulations is also weaker, owing to slower storm motions (Fig. 3), providing less opposing flow to any outflow (e.g., 20–30 m s^{-1} storm-relative inflow speeds in v20, v20p2, and v30p2 and 25–35 m s^{-1} storm-relative inflow speeds in b20, b20p2, and b30p2 at 80 min; not shown). For both of these reasons, outflow surges in

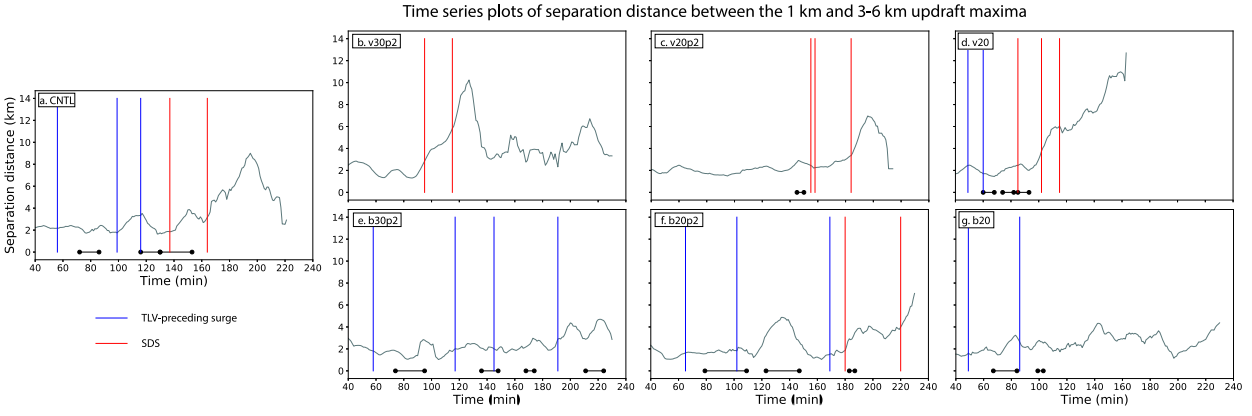

FIG. 16. The 10-min rolling average (centered on analysis time) of the separation distance (km) between the 1- and 3–6-km updraft maxima in the (a) CNTL, (b) v30p2, (c) v20p2, (d) v20, (e) b30p2, (f) b20p2, and (g) b20 simulations. Only times when the 2–5-km UH > 750 m^2 s^{-2} are considered in the rolling average and the time series end when no times in the rolling average meet the UH threshold. Vertical lines indicate TLV-preceding surges (blue) and SDSs (red). Horizontal black lines indicate the duration of TLVs. There was no outflow surge identified prior to the TLV in (c). There are only two TLV-preceding surges in (d) because the third TLV develops as the second TLV is occluded by the rear-flank gust front and a separate instigating outflow surge could not be identified.

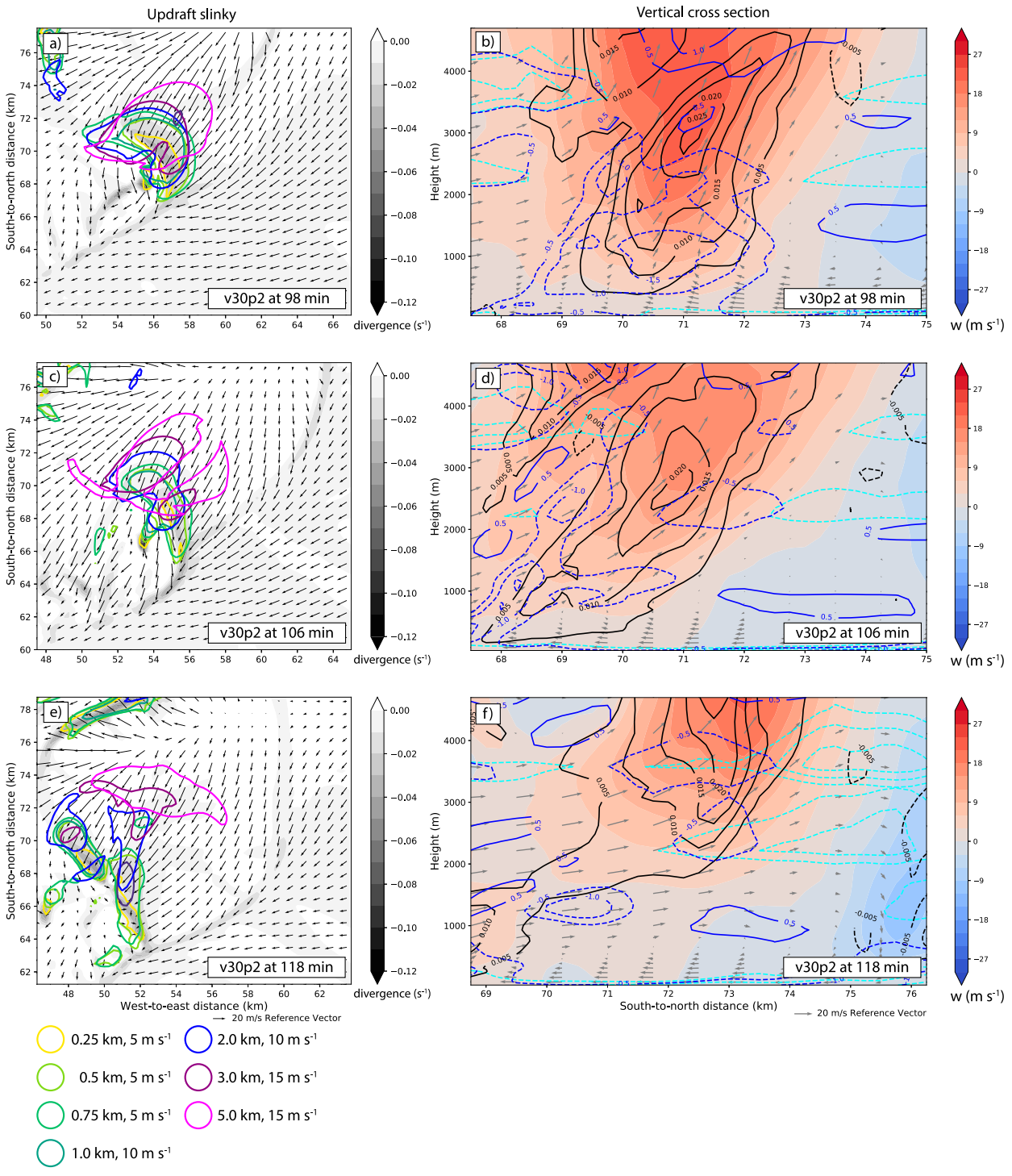

FIG. 17. (a) Updraft slinky depicting the updraft at 0.25 km (5 m s^{-1}), 0.5 km (5 m s^{-1}), 0.75 km (5 m s^{-1}), 1.0 km (10 m s^{-1}), 2.0 km (10 m s^{-1}), 3.0 km (15 m s^{-1}), and 5.0 km (15 m s^{-1}; contour color legend provided at the lower left), surface divergence (s^{-1}; shaded), and storm-relative winds (m s^{-1}; arrows) in the v30p2 simulation at 98 min. (b) South–north vertical cross section averaged over a 7.5 km × 7.5 km × 5 km box centered on the maximum 2–5-km updraft of vertical velocity (m s^{-1}; shaded), ζ (contour interval: 0.005 s^{-1}; positive values solid and negative values dashed black, zero contour omitted for clarity), $\partial p'/\partial z$ [contour interval: 0.5 hPa km^{-1}; positive values (downward) solid and negative values (upward) dashed blue, zero contour omitted for clarity], θ_ρ' (contoured every 1 K between −5 and −1 K; dashed cyan), and in-plane winds (m s^{-1}; arrows) in the v30p2 simulation at 98 min. (c),(d) As in (a) and (b), but at 106 min. (e),(f) As in (a) and (b), but at 118 min.

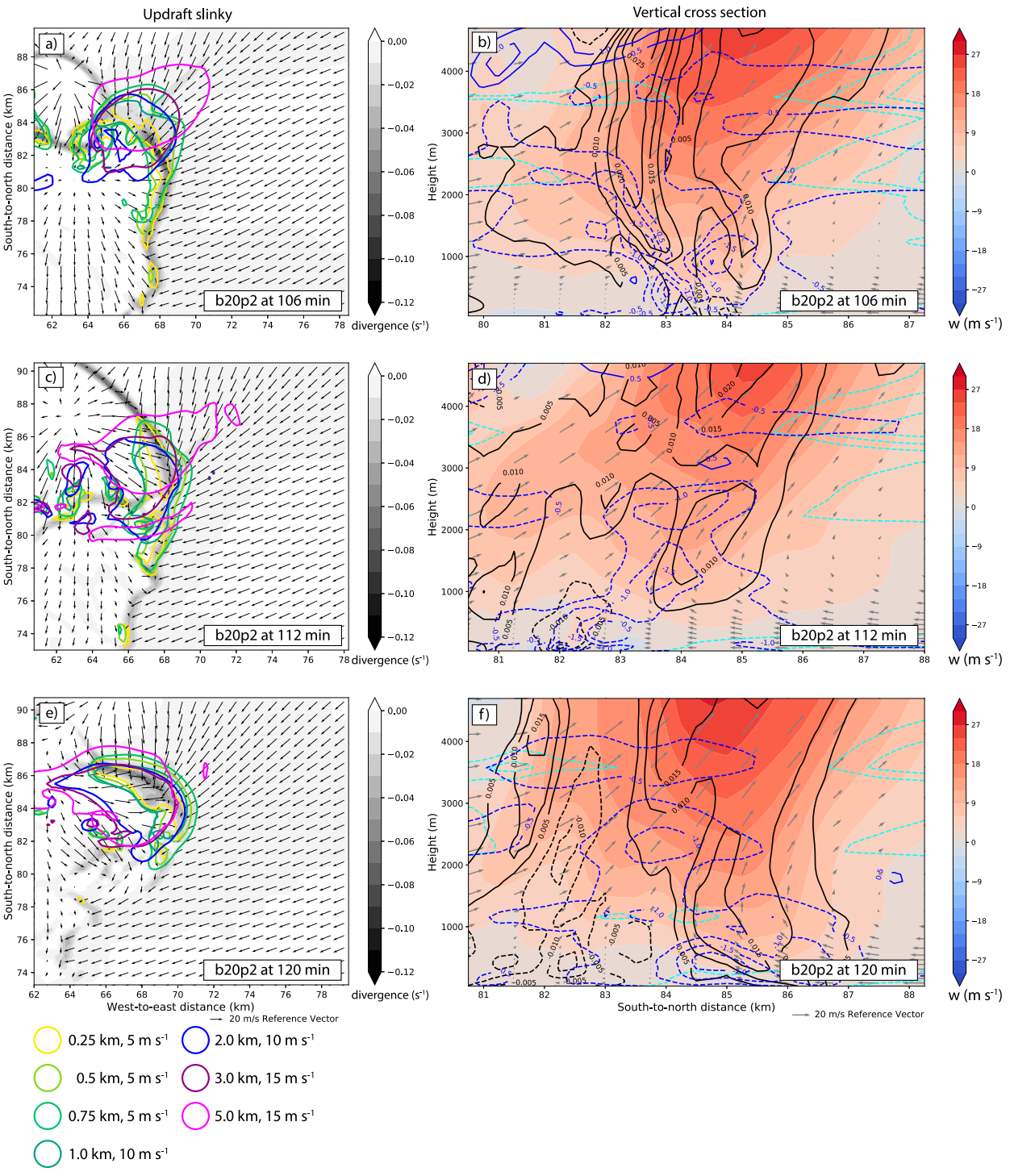

FIG. 18. As in Fig. 17, but for the b20p2 simulation at (a),(b) 106; (c),(d) 112; and (e),(f) 120 min.

the veering simulations are more likely to undercut the updrafts rather than aid in their maintenance.

As mentioned in section 3a, our results are more pronounced in the simulations using Morrison microphysics. The v20MOR and v30MOR simulations produce far fewer outflow surges than the other simulations (not shown), likely owing to early updraft dissipation in those simulations. By 100 min in v20MOR (Fig. 20a) and v30MOR (not shown) simulations, the forward-flank gust front is already 6–7 km south of the updraft because the Morrison microphysics yields earlier development

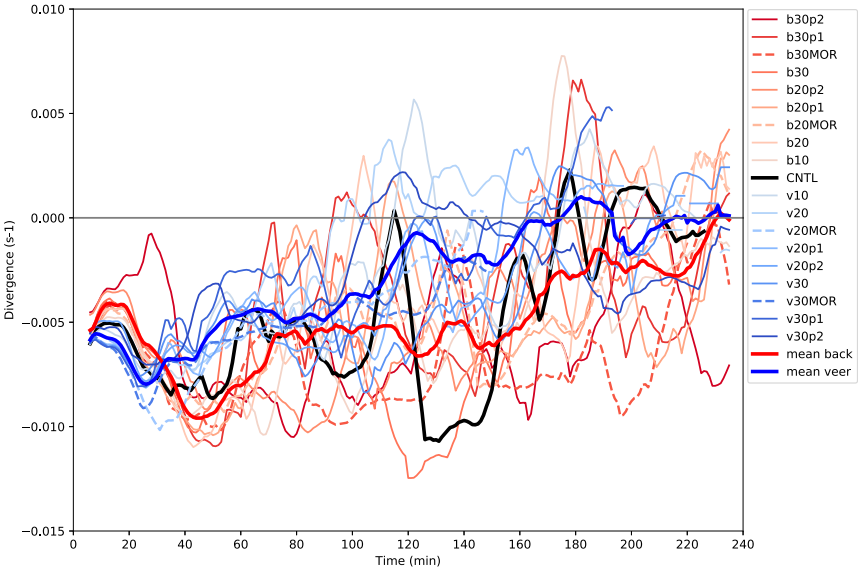

FIG. 19. The 10-min rolling average (centered on analysis time) of mean surface divergence (s^{-1}) within a 5 km × 5 km box centered on the 2–5-km maximum updraft in each simulation. Simulations using the Morrison microphysics are dashed. Thick lines are averages of all veering (blue) and backing (red) simulations. The thick black line is the 10-min rolling average of the CNTL simulation. Only times when the maximum 2–5-km UH > 750 $m^2 s^{-2}$ are considered for all averages.

of a larger and colder cold pool with more widespread outflow instead of localized surges (outflow within the forward flank is generally about 2 K colder in the Morrison simulations than in the other simulations; Fig. 20). Similar behavior was documented by Wade and Parker (2021) in their high-shear, low-CAPE supercell simulations using Morrison microphysics. This pattern exacerbates the reduction of convergence beneath an updraft in the veering simulations (Fig. 19). In the b20MOR (Fig. 20c) and b30MOR (not shown) simulations, a more widespread and colder cold pool also exists, but the forward-flank gust front does not travel as far southward because the outflow surges occur more in the rear flank of those storms, thus convergence persists beneath the updrafts, and the storms last longer.

4. Conclusions

By running a suite of idealized simulations in which the 3–6-km shear vector is systematically varied, we found that when the 3–6-km shear vector is backed, the simulated supercells persist longer and produce more and longer-lasting TLVs than when the 3–6-km shear vector is veered. Supercells in all of the simulations move slower than predicted by Bunkers et al. (2000), and backing simulation supercells maintain greater deviant rightward motion longer owing to stronger, more persistent updrafts which maintain upward LDPA on their right flanks, yielding more SRH available to these storms. Veering simulation supercells exhibit updrafts that weaken earlier, resulting in weaker upward LDPA on their right flanks, less deviant rightward motion, and thus less SRH with time.

Outflow surges in the backing simulations primarily occur northwest of the updrafts and generally do not disrupt inflow into or convergence beneath the updrafts, while outflow surges in the veering simulations occur more north or northeast of the updrafts and often result in negatively buoyant air disrupting the flow of warm moist air into the updrafts and the convergence beneath them. These preferred outflow surge locations may change slightly for other 0–3-km wind profiles, though we would not expect large changes provided similar 0–3-km shear. The presence of negatively buoyant air, which in these simulations is not all that cold (θ'_ρ around −2 K), in the inflow region of a storm may be less important, however, than the storm-relative location of outflow surges, which can strongly modulate the convergence beneath the updrafts. Outflow surges that result in storm dissipation persist slightly longer than those that do not, but not as long as TLV-preceding surges. SDSs are more common when mesocyclones are smaller and TLV-preceding surges are more common when mesocyclones are larger.

The storm-relative location of outflow surges is spatially related to the storm-relative location of the greatest 1–3-km precipitation loading across the entire suite of simulations. SDSs generally occur north or northeast of the updrafts, where surges are more common in the veering simulations. The mean θ'_ρ values at the center of outflow surges do not vary significantly between simulations (Table 1). Forward trajectories were calculated to investigate the θ'_ρ of outflow surge air as it flows toward the updrafts (since θ'_ρ values change as air moves away from an outflow surge center). There is not a significant difference in the mean θ'_ρ of the trajectories that pass beneath the updrafts between the veering (mean θ'_ρ of −1.6 K) and

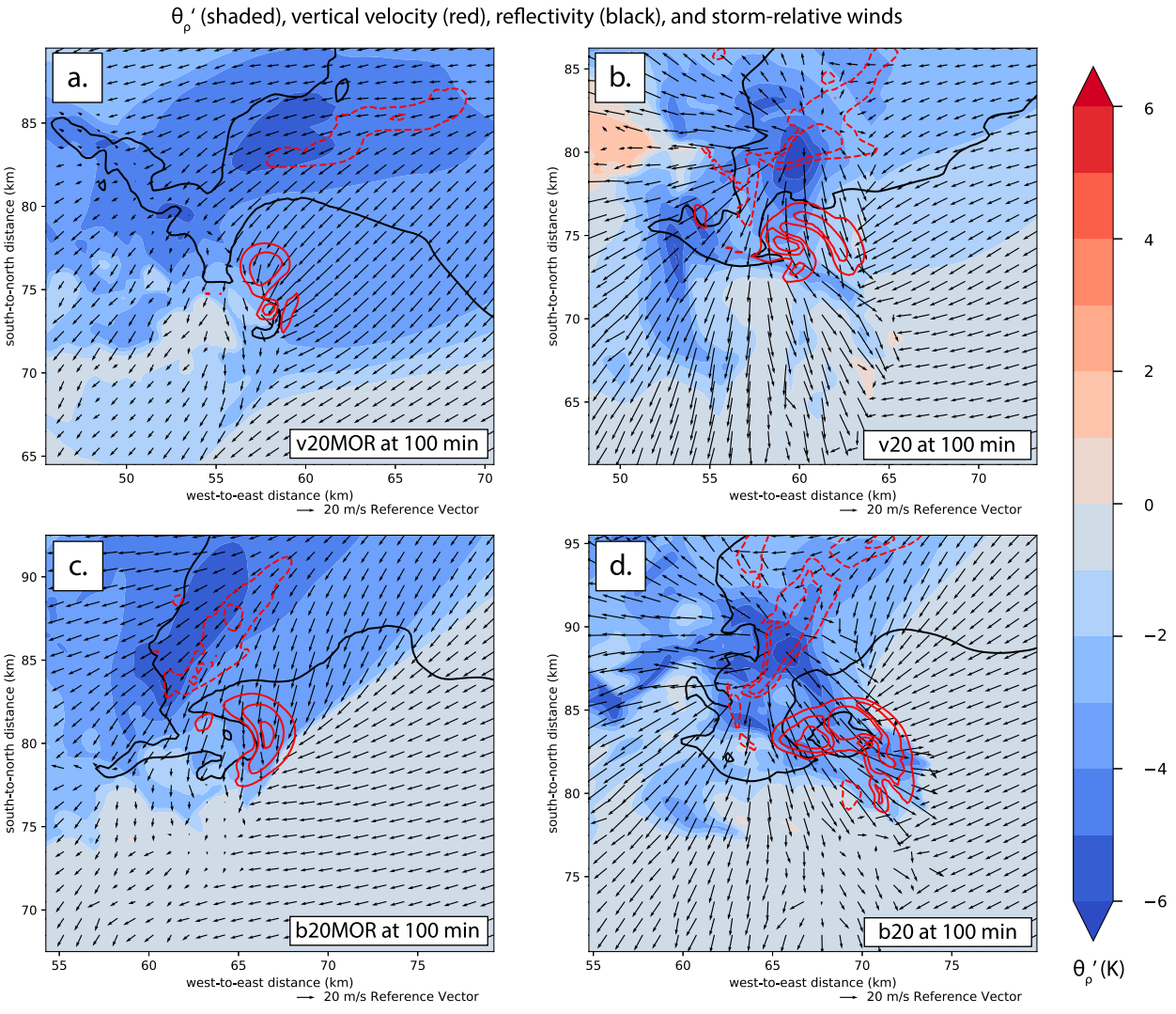

FIG. 20. Surface θ_ρ' (K; shaded), 1–3-km vertical velocity (−8, −4, 10, 15, and 20 m s^{-1}; red contours; negative values dashed and positive values solid), 40-dBZ reflectivity contour at 1 km (black), and surface storm-relative winds (arrows) in the (a) v20MOR, (b) v20, (c) b20MOR, and (d) b20 simulations at 100 min.

backing simulations (mean θ_ρ' of −2.3 K; Fig. 13 and Table 2), or between that of TLV-preceding surges (mean θ_ρ' of −2.4 K) and SDSs (mean θ_ρ' of −1.7 K; Fig. 13 and Table 2). Thus, the veering simulation supercells do not dissipate earlier owing to colder outflow. Backward trajectories were used to determine the mean net downward excursion of outflow surge air. The mean net downward excursion of trajectories that enter backing and veering simulation outflow surges and SDSs and TLV-preceding surges does not differ significantly. The net downward excursions of trajectories usually range between 0.5 and 2.0 km, consistent with previous studies.

SDSs precede or coincide with a weakening and tilting of low-level updrafts. As an SDS passes beneath an updraft, the low-level upward-directed $\partial p'/\partial z$ shifts south of the midlevel updraft, which becomes undercut by outflow. Veering simulation supercells are more likely to produce SDSs owing to outflow surges more readily occurring north or northeast of the updrafts in these storms, which generally yield less convergence beneath the updrafts and more negatively buoyant air in the inflow region of the storms. In the backing simulations, outflow surges northwest of the updrafts generally yield stronger convergence beneath the updrafts, and these surges are less likely to tilt the updrafts and disrupt the inflow. Such surges may briefly weaken the low-level updrafts, but because convergence and upward-directed $\partial p'/\partial z$ is maintained beneath the midlevel updrafts, these surges are less likely to result in storm dissipation than those that occur more in the forward flanks of the simulated storms. Simulations using the Morrison microphysics parameterization generally produce more widespread and colder outflow, leading to early undercutting and dissipation of the storms in the Morrison veering simulations.

This study explores one physical pathway by which backing of the midlevel shear vector may be beneficial for supercell longevity. Results could differ, however, with other 0–3-km wind profiles and/or thermodynamic profiles. Our simulated supercells are isolated in a homogeneous environment, and in reality, environmental heterogeneities and storm interactions may assert a more dominant role on supercell longevity. The results of this study suggest that the orientation of the midlevel shear vector may be a parameter to consider for supercell longevity when isolated supercells are present or expected.

Although we emphasize the differences between the veering and backing simulations, a similarity between them is that, regardless of the updraft-relative outflow surge location, the air within the outflow surges is characterized by large values of streamwise vorticity (approaching $0.1\,s^{-1}$) near the surface. Recent work by Rotunno et al. (2017) and Boyer and Dahl (2020) suggests that the horizontal stretching and subsequent tilting of this streamwise vorticity in the lowest 10 m may lead to appreciable near-surface ζ ($0.01\,s^{-1}$) and strengthening of the low-level mesocyclone. These processes require that the streamwise vorticity-rich air from the outflow be ingested by an updraft, rather than pass beneath it, which appears to be more likely in our backing simulations. Our simulations suggest that outflow air is more likely to be ingested by an updraft when outflow surges occur more toward the rear flank of a storm because near-surface convergence is stronger, the mesocyclone remains larger and stronger, and upward-directed $\partial p'/\partial z$ is maintained beneath an updraft, all of which is more likely in the backing simulations. In the veering simulations, the outflow surge air is more likely to pass beneath an updraft, reduce the convergence beneath it, shift the upward-directed $\partial p'/\partial z$ away from the midlevel updraft, and cause the supercells to dissipate earlier. Future analysis will be conducted on the simulations presented herein to investigate the above claims about the origin and ingestion of streamwise vorticity-rich outflow air. We will also investigate how ingestion of such air may strengthen a low-level mesocyclone or contribute to TLV production by calculating streamwise and vertical vorticity budgets along trajectories. These vorticity budgets can also be used to determine if there are storm-relative outflow surge locations that maximize the production of baroclinic vorticity as near-surface air flows toward an updraft. The impact of friction on our results will also be investigated by performing simulations including surface drag.

Acknowledgments. We are grateful to the University of Illinois Department of Atmospheric Sciences for financial support; Dr. Tom Gowan of the University of Utah for sharing his trajectory code; Drs. Robert Trapp, Stephen Nesbitt, and Brian Jewett of the University of Illinois for their comments on this work; and David Wojtowicz and Dr. Ken Patten of the University of Illinois for technical support. We also thank Dr. James Marquis and two other anonymous reviewers, whose comments helped to improve this manuscript. Plots were created using the Matplotlib Python library and the MetPy Python package (May et al. 2020).

Data availability statement. The CM1 (Bryan and Fritsch 2002) source code can be found at https://www2.mmm.ucar.edu/people/bryan/cm1/. The namelist files and input soundings used to initialize our simulations can be found at https://github.com/kevingray92/The_Impact_of_Midlevel_Shear_Orientation_namelists_soundings.

REFERENCES

Anderson-Frey, A., and H. Brooks, 2019: Tornado fatalities: An environmental perspective. *Wea. Forecasting*, **34**, 1999–2015, https://doi.org/10.1175/WAF-D-19-0119.1.

Beck, J. R., and C. C. Weiss, 2013: An assessment of low-level baroclinity and vorticity within a simulated supercell. *Mon. Wea. Rev.*, **141**, 649–669, https://doi.org/10.1175/MWR-D-11-00115.1.

Bluestein, H. B., and M. L. Weisman, 2000: The interaction of numerically simulated supercells initiated along lines. *Mon. Wea. Rev.*, **128**, 3128–3149, https://doi.org/10.1175/1520-0493(2000)128<3128:TIONSS>2.0.CO;2.

Boyer, C. H., and J. M. L. Dahl, 2020: The mechanisms responsible for large near-surface vertical vorticity within simulated supercells and quasi-linear storms. *Mon. Wea. Rev.*, **148**, 4281–4297, https://doi.org/10.1175/MWR-D-20-0082.1.

Brooks, H. E., and Coauthors, 2019: A century of progress in severe convective storm research and forecasting. *A Century of Progress in Atmospheric and Related Sciences: Celebrating the American Meteorological Society Centennial*, *Meteor. Monogr.*, No. 59, 18.1–18.41, https://doi.org/10.1175/AMSMONOGRAPHS-D-18-0026.1.

Brown, M., and C. J. Nowotarski, 2019: The influence of lifting condensation level on low-level outflow and rotation in simulated supercell thunderstorms. *J. Atmos. Sci.*, **76**, 1349–1372, https://doi.org/10.1175/JAS-D-18-0216.1.

Browning, K. A., and G. B. Foote, 1976: Airflow and hail growth in supercell storms and some implications for hail suppression. *Quart. J. Roy. Meteor. Soc.*, **102**, 499–533, https://doi.org/10.1002/qj.49710243303.

Bryan, G. H., and J. M. Fritsch, 2002: A benchmark simulation for moist nonhydrostatic numerical models. *Mon. Wea. Rev.*, **130**, 2917–2928, https://doi.org/10.1175/1520-0493(2002)130<2917:ABSFMN>2.0.CO;2.

Bunkers, M. J., B. A. Klimowski, J. W. Zeitler, R. L. Thompson, and M. L. Weisman, 2000: Predicting supercell motion using a new hodograph technique. *Wea. Forecasting*, **15**, 61–79, https://doi.org/10.1175/1520-0434(2000)015<0061:PSMUAN>2.0.CO;2.

——, M. R. Hjelmfelt, and P. L. Smith, 2006: An observational examination of long-lived supercells. Part I: Characteristics, evolution, and demise. *Wea. Forecasting*, **21**, 673–688, https://doi.org/10.1175/WAF949.1.

Coffer, B. E., M. D. Parker, J. M. Dahl, L. J. Wicker, and A. J. Clark, 2017: Volatility of tornadogenesis: An ensemble of simulated nontornadic and tornadic supercells in VORTEX2 environments. *Mon. Wea. Rev.*, **145**, 4605–4625, https://doi.org/10.1175/MWR-D-17-0152.1.

——, M. Taszarek, and M. D. Parker, 2020: Near-ground wind profiles of tornadic and nontornadic environments in the United States and Europe from ERA5 reanalyses. *Wea. Forecasting*, **35**, 2621–2638, https://doi.org/10.1175/WAF-D-20-0153.1.

Coniglio, M. C., and M. D. Parker, 2020: Insights into supercells and their environments from three decades of targeted radiosonde observations. *Mon. Wea. Rev.*, **148**, 4893–4915, https://doi.org/10.1175/MWR-D-20-0105.1.

Dahl, J. M. L., 2015: Near-ground rotation in simulated supercells: On the robustness of the baroclinic mechanism. *Mon. Wea. Rev.*, **143**, 4929–4942, https://doi.org/10.1175/MWR-D-15-0115.1.

——, M. D. Parker, and L. J. Wicker, 2014: Imported and storm-generated near-ground vertical vorticity in a simulated supercell. *J. Atmos. Sci.*, **71**, 3027–3051, https://doi.org/10.1175/JAS-D-13-0123.1.

Davies-Jones, R., and H. E. Brooks, 1993: Mesocyclogenesis from a theoretical perspective. *The Tornado: Its Structure, Dynamics, Prediction, and Hazards*, C. Church et al., Eds., Amer. Geophys. Union, 105–114, https://doi.org/10.1029/GM079p0105.

Dial, G. L., J. P. Racy, and R. L. Thompson, 2010: Short-term convective mode evolution along synoptic boundaries. *Wea. Forecasting*, **25**, 1430–1446, https://doi.org/10.1175/2010WAF2222315.1.

Erwin, A., J. W. Frame, and G. Marion, 2016: Further analysis and verification of Storm Prediction Center 1300 UTC Tornado Outlooks. *28th Conf. on Severe Local Storms*, Portland, OR, Amer. Meteor. Soc., P96, https://ams.confex.com/ams/28SLS/webprogram/Paper301752.html.

Finley, C. A., and B. D. Lee, 2004: High resolution mobile mesonet observations of RFD surges in the June 9 Basset, Nebraska, supercell during Project ANSWERS 2003. *22nd Conf. on Severe Local Storms*, Hyannis, MA, Amer. Meteor. Soc., P11.3, https://ams.confex.com/ams/11aram22sls/techprogram/paper_82005.htm.

——, L. Orf, B. D. Lee, and R. B. Wilhelmson, 2018: High-resolution simulation of a violent tornado in the 27 April 2011 outbreak environment. *29th Conf. on Severe Local Storms*, Stowe, VT, Amer. Meteor. Soc., P10B.5, https://ams.confex.com/ams/29SLS/webprogram/Paper348812.html.

Flournoy, M. D., M. C. Coniglio, E. N. Rasmussen, J. C. Furtado, and B. E. Coffer, 2020: Modes of storm scale variability and tornado potential in VORTEX2 near- and far-field tornadic environments. *Mon. Wea. Rev.*, **148**, 4185–4207, https://doi.org/10.1175/MWR-D-20-0147.1.

Glass, F. H., and M. F. Britt, 2002: The historic Missouri–Illinois high precipitation supercell of 10 April 2001. Preprints, *21st Conf. on Severe Local Storms*, San Antonio, TX, Amer. Meteor. Soc., 99–104.

Guarriello, F., C. J. Nowotarski, and C. C. Epifanio, 2018: Effects of the low-level wind profile on outflow position and near-surface vertical vorticity in simulated supercell thunderstorms. *J. Atmos. Sci.*, **75**, 731–753, https://doi.org/10.1175/JAS-D-17-0174.1.

Klees, A. M., Y. P. Richardson, P. M. Markowski, C. Weiss, J. M. Wurman, and K. K. Kosiba, 2016: Comparison of the tornadic and nontornadic supercells intercepted by VORTEX2 on 10 June 2010. *Mon. Wea. Rev.*, **144**, 3201–3231, https://doi.org/10.1175/MWR-D-15-0345.1.

Knupp, K. R., and Coauthors, 2014: Meteorological overview of the devastating 27 April 2011 tornado outbreak. *Bull. Amer. Meteor. Soc.*, **95**, 1041–1062, https://doi.org/10.1175/BAMS-D-11-00229.1.

Kosiba, K., J. Wurman, Y. Richardson, P. Markowski, P. Robinson, and J. Marquis, 2013: Genesis of the Goshen County, Wyoming, Tornado on 5 June 2009 during VORTEX2. *Mon. Wea. Rev.*, **141**, 1157–1181, https://doi.org/10.1175/MWR-D-12-00056.1.

Lee, B. D., C. A. Finley, and C. D. Karstens, 2012: The Bowdle, South Dakota, cyclic tornadic supercell of 22 May 2010: Surface analysis of rear-flank downdraft evolution and multiple internal surges. *Mon. Wea. Rev.*, **140**, 3419–3441, https://doi.org/10.1175/MWR-D-11-00351.1.

Lemon, L. R., and C. A. Doswell III, 1979: Severe thunderstorm evolution and mesocyclone structure as related to tornadogenesis. *Mon. Wea. Rev.*, **107**, 1184–1197, https://doi.org/10.1175/1520-0493(1979)107<1184:STEAMS>2.0.CO;2.

Mansell, E. R., 2010: On sedimentation and advection in multi-moment bulk microphysics. *J. Atmos. Sci.*, **67**, 3084–3094, https://doi.org/10.1175/2010JAS3341.1.

——, C. L. Ziegler, and E. C. Bruning, 2010: Simulated electrification of a small thunderstorm with two-moment bulk microphysics. *J. Atmos. Sci.*, **67**, 171–194, https://doi.org/10.1175/2009JAS2965.1.

Markowski, P. M., 2020: What is the intrinsic predictability of tornadic supercell thunderstorms? *Mon. Wea. Rev.*, **148**, 3157–3180, https://doi.org/10.1175/MWR-D-20-0076.1.

——, and Y. P. Richardson, 2017: Large sensitivity of near-surface vertical vorticity development to heat sink location in idealized simulations of supercell-like storms. *J. Atmos. Sci.*, **74**, 1095–1104, https://doi.org/10.1175/JAS-D-16-0372.1.

——, J. M. Straka, and E. N. Rasmussen, 2002: Direct surface thermodynamic observations within the rear-flank downdrafts of nontornadic and tornadic supercells. *Mon. Wea. Rev.*, **130**, 1692–1721, https://doi.org/10.1175/1520-0493(2002)130<1692:DSTOWT>2.0.CO;2.

Marquis, J., Y. Richardson, P. Markowski, D. Dowell, and J. Wurman, 2012: Tornado maintenance investigated with high-resolution dual-Doppler and EnKF analysis. *Mon. Wea. Rev.*, **140**, 3–27, https://doi.org/10.1175/MWR-D-11-00025.1.

——, ——, ——, J. Wurman, K. Kosiba, and P. Robinson, 2016: An investigation of the Goshen County, Wyoming, tornadic supercell of 5 June 2009 using EnKF assimilation of mobile mesonet and radar observations collected during VORTEX2. Part II: Mesocylone-scale processes affecting tornado formation, maintenance, and decay. *Mon. Wea. Rev.*, **144**, 3441–3463, https://doi.org/10.1175/MWR-D-15-0411.1.

May, R. M., S. C. Arms, P. Marsh, E. Bruning, J. R. Leeman, K. Goebbert, J. E. Thielen, and Z. Bruick, 2020: MetPy: A Python Package for Meteorological Data. Unidata, accessed 15 December 2020, https://doi.org/10.5065/D6WW7G29.

Miltenberger, A. K., S. Pfahl, and H. Wernli, 2013: An online trajectory module (version 1.0) for the nonhydrostatic numerical weather prediction model COSMO. *Geosci. Model Dev.*, **6**, 1989–2004, https://doi.org/10.5194/gmd-6-1989-2013.

Morrison, H., J. A. Curry, and V. Khvorostyanov, 2005: A new double-moment microphysics parameterization for application in cloud and climate models. Part I: Description. *J. Atmos. Sci.*, **62**, 1665–1677, https://doi.org/10.1175/JAS3446.1.

Naylor, J., and M. S. Gilmore, 2012: Convective initiation in an idealized cloud model using an updraft nudging technique. *Mon. Wea. Rev.*, **140**, 3699–3705, https://doi.org/10.1175/MWR-D-12-00163.1.

Orf, L., R. Wilhelmson, B. Lee, C. Finley, and A. Houston, 2017: Evolution of a long-track violent tornado within a simulated supercell. *Bull. Amer. Meteor. Soc.*, **98**, 45–68, https://doi.org/10.1175/BAMS-D-15-00073.1.

Parker, M. D., 2017: How much does "backing aloft" actually impact a supercell? *Wea. Forecasting*, **32**, 1937–1957, https://doi.org/10.1175/WAF-D-17-0064.1.

Peters, J. M., C. J. Nowotarski, J. P. Mulholland, and R. L. Thompson, 2020: The influences of effective inflow layer streamwise vorticity and storm-relative flow on supercell updraft properties. *J. Atmos. Sci.*, **77**, 3033–3057, https://doi.org/10.1175/JAS-D-19-0355.1.

Riganti, C. J., and A. L. Houston, 2017: Rear-flank outflow dynamics and thermodynamics in the 10 June 2010 Last Chance,

Colorado, supercell. *Mon. Wea. Rev.*, **145**, 2487–2504, https://doi.org/10.1175/MWR-D-16-0128.1.

Rotunno, R., and J. B. Klemp, 1982: The influence of the shear-induced pressure gradient on thunderstorm motion. *Mon. Wea. Rev.*, **110**, 136–151, https://doi.org/10.1175/1520-0493(1982)110<0136:TIOTSI>2.0.CO;2.

——, and ——, 1985: On the rotation and propagation of simulated supercell thunderstorms. *J. Atmos. Sci.*, **42**, 271–292, https://doi.org/10.1175/1520-0469(1985)042<0271:OTRAPO>2.0.CO;2.

——, P. M. Markowski, and G. H. Bryan, 2017: "Near ground" vertical vorticity in supercell thunderstorm models. *J. Atmos. Sci.*, **74**, 1757–1766, https://doi.org/10.1175/JAS-D-16-0288.1.

Schenkman, A. D., M. Xue, and M. Hu, 2014: Tornadogenesis in a high-resolution simulation of the 8 May 2003 Oklahoma City supercell. *J. Atmos. Sci.*, **71**, 130–154, https://doi.org/10.1175/JAS-D-13-073.1.

——, ——, and D. T. Dawson, 2016: The cause of internal outflow surges in a high-resolution simulation of the 8 May 2003 Oklahoma City tornadic supercell. *J. Atmos. Sci.*, **73**, 353–370, https://doi.org/10.1175/JAS-D-15-0112.1.

Schoen, J., and W. Ashley, 2011: A climatology of fatal convective wind events by storm type. *Wea. Forecasting*, **26**, 109–121, https://doi.org/10.1175/2010WAF2222428.1.

Skinner, P. S., C. C. Weiss, M. M. French, H. B. Bluestein, P. M. Markowski, and Y. P. Richardson, 2014: VORTEX2 observations of a low-level mesocyclone with multiple internal rear-flank downdraft momentum surges in the 18 May 2010 Dumas, Texas, supercell. *Mon. Wea. Rev.*, **142**, 2935–2960, https://doi.org/10.1175/MWR-D-13-00240.1.

——, ——, L. J. Wicker, C. K. Potvin, and D. C. Dowell, 2015: Forcing mechanisms for an internal rear-flank downdraft momentum surge in the 18 May 2010 Dumas, Texas, supercell. *Mon. Wea. Rev.*, **143**, 4305–4330, https://doi.org/10.1175/MWR-D-15-0164.1.

Thompson, R. L., R. Edwards, J. A. Hart, K. L. Elmore, and P. Markowski, 2003: Close proximity soundings within supercell environments obtained from the Rapid Update Cycle. *Wea. Forecasting*, **18**, 1243–1261, https://doi.org/10.1175/1520-0434(2003)018<1243:CPSWSE>2.0.CO;2.

——, ——, and C. M. Mead, 2004: An update to the supercell composite and significant tornado parameters. *22nd Conf. on Severe Local Storms*, Hyannis, MA, Amer. Meteor. Soc., P8.1.

Trapp, R. J., G. R. Marion, and S. W. Nesbitt, 2017: The regulation of tornado intensity by updraft width. *J. Atmos. Sci.*, **74**, 4199–4211, https://doi.org/10.1175/JAS-D-16-0331.1.

Vande Guchte, A., and J. M. L. Dahl, 2018: Sensitivities of parcel trajectories beneath the lowest scalar model level of a Lorenz vertical grid. *Mon. Wea. Rev.*, **146**, 1427–1435, https://doi.org/10.1175/MWR-D-17-0190.1.

Wade, A. R., and M. D. Parker, 2021: Dynamics of simulated high-shear low-CAPE supercells. *J. Atmos. Sci.*, **78**, 1389–1410, https://doi.org/10.1175/JAS-D-20-0117.1.

Warren, R. A., H. Richter, H. A. Ramsay, S. T. Siems, and M. J. Manton, 2017: Impact of variations in upper-level shear on simulated supercells. *Mon. Wea. Rev.*, **145**, 2659–2681, https://doi.org/10.1175/MWR-D-16-0412.1.

Ziegler, C. L., 1985: Retrieval of thermal and microphysical variables in observed convective storms. Part I: Model development and preliminary testing. *J. Atmos. Sci.*, **42**, 1487–1509, https://doi.org/10.1175/1520-0469(1985)042<1487:ROTAMV>2.0.CO;2.